Incoherent π^0 photoproduction in the PrimEx kinematics via the MCMC intranuclear cascade model (PrimEx Note 52)

Tulio E. Rodrigues

University of São Paulo, São Paulo, Brazil (tulio@if.usp.br)

September 5, 2008

Abstract

The nuclear incoherent π^0 photoproduction cross sections from Carbon and Lead at forward angles are calculated within the PrimEx kinematics using an extended version of the MultiCollisional Monte Carlo intranuclear cascade model (MCMC). The model uses relativistic kinematics and takes into account the elementary photoproduction from the nucleon and the in-medium effects due to short range correlations, as well as the pion-nucleus Final State Interactions (FSI) in terms of a multiple-scattering and time dependent framework. The single and double differential cross sections are calculated in order to provide a consistent interpretation of the inelastic background of the PrimEx experiment at the Jefferson Laboratory Facility. The attenuation of the nuclear cross sections due to π^0 absorption and re-scattering reproduces very accurately previous measurement from Cornell after the inclusion of shadowing effects of the incoming photon.

Contents

1 INTRODUCTION

The PrimEx experiment[1] at the Jefferson Laboratory Facility (JLab) is currently performing a high precision measurement of the $\pi^0 \rightarrow \gamma\gamma$ decay width via the Primakoff cross section[2]. The method, which was first proposed by Primakoff, propitiates the determination of the decay width by the magnitude of the electromagnetic component of the π^0 differential cross section at forward angles. However, additionally to the Coulomb contribution, neutral pions can also be produced in the strong field of complex nuclei either coherently or incoherently. The incoherent photoproduction is described as an incoherent sum of nucleon amplitudes and is associated with a final state of a π^0 plus an excited nucleus. Such complicated mechanism depends very critically on the photoproduction process, as well as on the Final State Interactions (FSI) of the produced mesons on their way out of the nucleus. The calculation of the nuclear amplitude can be performed using the multiple-scattering integral formalism developed by Glauber[3]. The model is based on the Eikonal approximation and consists of a powerful theoretical approach to evaluate the nuclear absorption of mesons. However, the Galuber method has some limitations since it does not account for the short range correlations and the local density fluctuation caused by the hadron-nucleus interaction. The short range correlations are not expected to play a major role in high energy nuclear reactions, except for *soft* πN scatterings that may affect the π^0 photoproduction cross sections at forward angles, the main focus of the PrimEx experiment. Furthermore, the Glauber model does not account for the energy losses during the π^0 photoproduction and also at any given πN binary scattering. Other restrictions of the analytical approach are associated with the inclusion of accurate physical ingredients to describe the structure of light nuclei, such as the momentum distribution of the bound nucleons; as well as the inclusion of kinematical constraints that propitiates the compatibility between theory and experiment.

The MCMC (Monte Carlo MultiCollisional) intranuclear cascade model consists of a relativistic and time-dependent Monte Carlo algorithm that describes the dynamics of an excited nuclear ensemble in terms of successive and time ordered binary collisions. This approach uses the concept of interaction probability, instead of scattering amplitude, and is expected to work very efficiently if the relative motion of the colliding particles can be separated from the rest of the nuclear wave function, which acts as a spectator during the interaction time. Such condition is perfectly fulfilled in the PrimEx kinematics, where the pions to be transported in the nuclear medium have total energy typically within 4.5 to 5.8 GeV.

It is also important to make salient that the MCMC and Galuber models have advantages and disadvantages and a direct comparison between their predictions is extremely important in order to provide two distinct and independent solutions for the inelastic background of the PrimEx experiment. The calculations of the incoherent cross section using the Glauber model are described elsewhere[4].

An extended version of the MCMC cascade[5] has been successfully applied for the interpretation of the recent data of incoherent π^0 photoproduction near the Delta resonance for ^{12}C and ^{208}Pb obtained at the Mainz Microton Facility[6]. In this work, we have also calculated incoherent π^0 photoproduction from ^{12}C and ^{208}Pb within 4.0 to 6.0 GeV in order to provide theoretical support for the Collaboration. This version was implemented neglecting shadowing effects of the incoming photon and assuming an isotropic angular distribution for the elastic $\pi^0 N$ scattering. Coherent production (electromagnetic/nuclear) of neutral pions was also investigated in a recent paper[7] taking into account the relativistic recoil of the nucleus. The calculations of the pion spectra due to coherent production showed that those mechanisms are largely concentrated within the quasi-elastic peak, with the total energy of the mesons being typically within the photon energy k and $k - 10$

MeV.

Low energy photonuclear reactions in a wide range of target nuclei were also investigated in other versions of the MCMC model dedicated to the quasideuteron channel[8, 9]. These works provided a completely new approach for the implementation of the Pauli-blocking mechanism using a non-stochastic method.

The MCMC model was also recently applied for the calculation of the η photoproduction cross sections from Be and Cu around 9.0 GeV[10], following the same steps developed for the case of π^0. This paper showed that the inelastic background in the photoproduction yields obtained at Cornell[11] is completely interpreted as the nuclear incoherent (NI) cross section for single η production.

In this work, I report improved calculations for the incoherent π^0 photoproduction cross section from ^{12}C and ^{208}Pb within the PrimEx kinematics. The basic features and improvements of the MCMC cascade model are: i) the use of a time dependent multicollisional relativistic kinematics, ii) the inclusion of the π^0 photoproduction mechanism within 4.0 to 6.0 GeV in terms of ρ and ω exchange, iii) the incorporation of an accurate momentum distribution for ^{12}C based on the global $1s$ and $1p$ proton knock-out data, iv) a rigorous non-stochastic Pauli-blocking both for the photoproduction and multiple $\pi^0 N$ scatterings, v) the implementation of the shadowing effects during the photo-nucleus interaction in terms of the VMD model with formation time constraint, and vi) a consistent analysis of the full Final State Interactions of the produced mesons with the nucleus, as well as the use of a realistic (diffractive) angular distribution for the $\pi^0 N$ elastic scattering.

2 π^0 PHOTOPRODUCTION FROM THE NUCLEON

The elementary π^0 photoproduction from a single nucleon is represented by the following process:

$$\gamma(k) + N(p_1) \rightarrow \pi^0(p) + N(p_2), \tag{1}$$

where k, p_1, p and p_2 represent the 4-momentum of the incoming photon, struck nucleon, produced pion and outgoing nucleon, respectively.

Following the same steps delineated in ref.[5], we can calculate the differential cross section for meson photoproduction from the nucleon at small angles in the center of mass of the $s-$channel as[12]:

$$\left(\frac{d\sigma}{d\Omega}\right)_N \cong |f_1 - f_2|^2 + \frac{\theta^{*2}}{2}\left[|f_3 + f_4|^2 + 2\,\mathrm{Re}\left(f_1^* f_2 + f_1^* f_4 + f_2^* f_3\right)\right], \tag{2}$$

where the f_i's are the Pauli-type amplitudes[13]. These amplitudes are functions of the invariant amplitudes $A_i = A_i(s,t)$, with $s = (k+p_1)^2$ and $t = (k-p)^2$ representing the Mandelstam variables. The relationship between the Pauli-type amplitudes f_i's and the analytical amplitudes A_i's is given by[12, 13], where we have assumed that the initial and final nucleon energies are the same ($t \ll 1$).

By decomposing the invariant amplitudes A_i in terms of regularized and parity-conserving t-channel helicity amplitudes F_i, we obtain[14, 15]:

$$A_1 = -\frac{tF_1 + 2m_N F_3}{t - 4m_N^2} \tag{3}$$

$$A_2 = \frac{F_1}{t - 4m_N^2} + \frac{1}{t}\left[F_2 + \frac{2m_N F_3}{t - 4m_N^2}\right] \tag{4}$$

$$A_3 = -F_4 \tag{5}$$

$$A_4 = -\frac{2m_N F_1 + F_3}{t - 4m_N^2}, \tag{6}$$

where m_N is the nucleon mass.

The amplitudes F_2 (unnatural parity exchange) and F_3 (natural parity exchange) receive contributions from different trajectories, while the amplitudes A_i are known to be free of kinematical singularities[12]. Since eq.(4) has a pole at $t = 0$, one is forced to postulate the so-called "conspiracy relation" at zero momentum transfer([1]):

$$F_3(s, t = 0) = 2m_N F_2(s, t = 0). \tag{7}$$

So, using eqs.(3 - 7) and writing eq.(2) in terms of the F_i's, we have[14]:

$$\left(\frac{d\sigma}{dt}\right)_N = \frac{\pi}{p^2}\left(\frac{d\sigma}{d\Omega}\right)_N = \frac{1}{32\pi}\left\{\frac{F_3^2}{2m_N^2} - \left[t + \left(\frac{m_\pi^2}{2k}\right)^2\right]\left[F_4^2 + \frac{F_1^2}{4m_N^2} + \frac{F_3^2}{16m_N^4} + \frac{F_1 F_3}{2m_N}\frac{1}{p\sqrt{s}}\right]\right\}, \tag{8}$$

where m_π is the meson mass.

The helicity amplitudes F_i are then calculated using the Regge model, including ω and ρ mesons

[1] This relation is similar to the one obtained by Ball *et al.*[15]. The difference comes from the pion exchange, which does not contribute for π^0 production.

trajectories and taking into account the reggeon cuts[16]. Within this approach, the amplitudes F_i lose the property of definite parity and also become finite at zero momentum transfer. The photon exchange amplitude F^C, which is the elementary Primakoff effect, plays an essential role at low momentum transfer and is included for fitting the data. However, since we are particularly interested in the NI cross section, one has to subtract the Coulomb term in order to feed the cascade input only with the strong part of the photoproduction amplitude. This procedure assures that the Impulse Approximation (IA) holds for the description of the NI cross section from complex nuclei, which is assumed to be proportional to the cross section from a single nucleon. So, the effects of the remaining $A-1$ nucleons can be safely neglected in the photoproduction mechanism. The IA obviously breaks down for the case of Coulomb interaction, which can not be constrained within the nucleon dimension, interfering with the Coulomb fields of the remaining nucleons. This γ^*- nucleus interaction, which is no longer interpreted as a two-body mechanism, can be coherent (Primakoff) or incoherent (excited nucleus), but the later is strongly Pauli suppressed since the Coulomb amplitude goes as $\frac{1}{t}$.

So, neglecting B-exchange ($F_4 = 0$) and adding constructively the cuts and Coulomb contributions, we have[14, 16]:

$$F_1 \rightarrow F_1 + F_1^{cut} + F_1^C, F_3 \rightarrow F_3^{cut}, \tag{9}$$

where:

$$F_1(s,t) = \frac{\sqrt{2}}{m_N}\gamma_1 \frac{1-e^{-i\pi\alpha(t)}}{\sin\left[\pi\alpha(t)\right]}\alpha(t)\left[1+\alpha(t)\right]\left[2+\alpha(t)\right]\left(\frac{s}{s_0}\right)^{\alpha(t)-1}, \tag{10}$$

$$F_1^{cut}(s,t) = \frac{\sqrt{2}}{m_N}\gamma_1^{cut}\frac{1-e^{-i\pi\alpha(0)}}{\sin\left[\pi\alpha(0)\right]}\left(\frac{s}{s_0}\right)^{\alpha(0)-1}\frac{e^{at}}{\ln\left(\frac{s}{s_0}\right)}, \tag{11}$$

$$F_1^{C}(s,t) = -\frac{2m_N}{t}0.0543\sqrt{\Gamma_{\gamma\gamma}}G_E(t), \text{ and}$$

$$F_3^{cut}(s,t) = 2\sqrt{2}\gamma_3^{cut}\frac{1-e^{-i\pi\alpha(0)}}{\sin\left[\pi\alpha(0)\right]}\left(\frac{s}{s_0}\right)^{\alpha(0)-1}\frac{e^{at}}{\ln\left(\frac{s}{s_0}\right)}. \tag{12}$$

The Regge trajectories were taken as $\alpha_{\omega,\rho}(t) = 0.45 + 0.9t$, with $s_0 = 1$ GeV^2. The parameters $\gamma_1 = 115.4(3.7)\sqrt{\mu b}, \gamma_1^{cut} = 55.2(5.7)\sqrt{\mu b}$, $\gamma_3^{cut} = 13.5(0.8)\frac{\sqrt{\mu b}}{GeV}$, $a = 1.20$ GeV^{-2} ([2]) and $\Gamma_{\gamma\gamma} = 8.44$ eV represent the best fit values to the available experimental data[16]; $G_E(t)$ is the electric dipole proton form factor ([3]).

The results of the elementary photoproduction parameterization with and without the Coulomb contribution are shown in figure 1. The data were taken from [16, 17] and the solid histograms represent our Monte Carlo generated input.

[2] This value is slightly higher than the value of Ref. [16] in order to improve our fitting at larger angles.

[3] The magnetic part of the Coulomb amplitude goes with t and does not contribute significantly for low scattering angles.

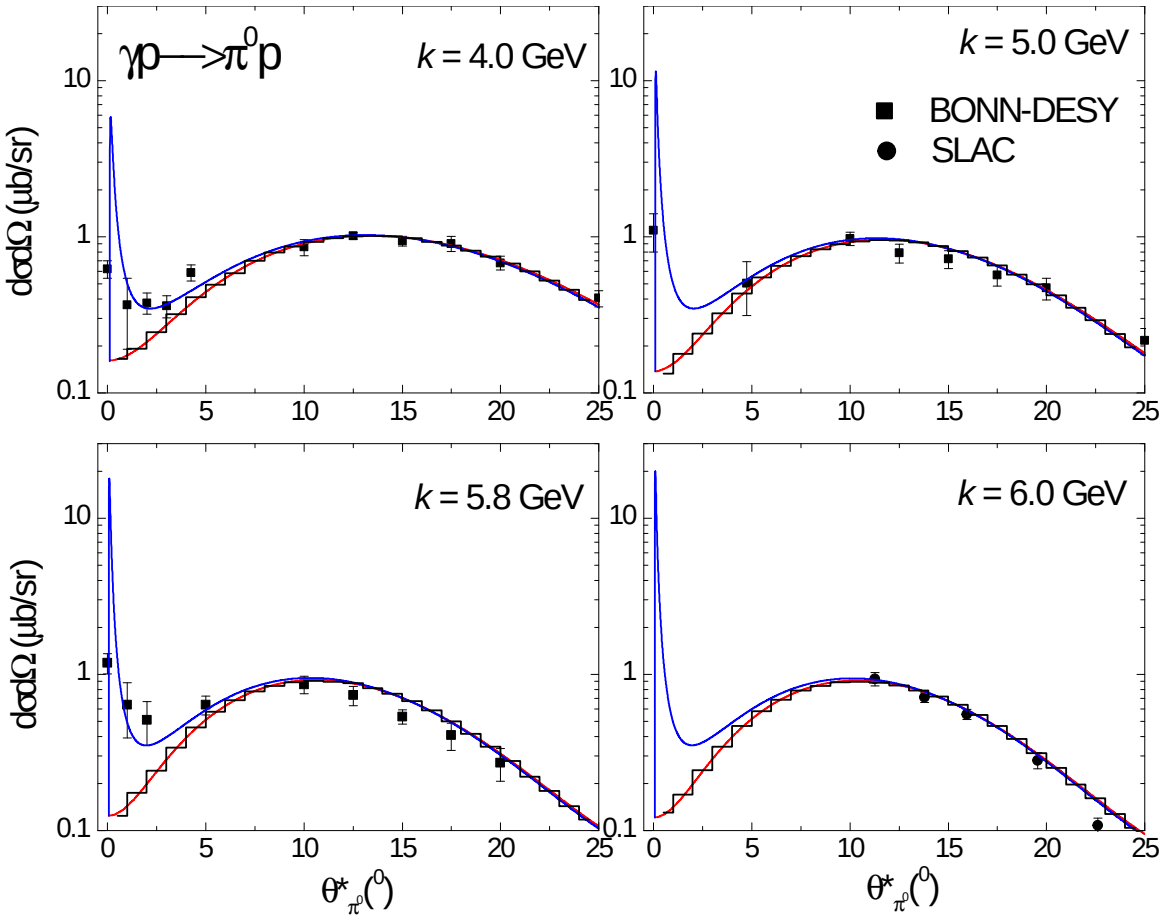

Figure 1: Differential cross section for π^0 photoproduction from the proton. The blue lines include the strong (red) and the Coulomb contributions to the cross section. The solid histograms are the cascade inputs, which take into account only the strong part. The data points were taken from refs.[16] (squares) and[17] (circles).

Figure 2 presents our parameterization for the differential cross section for π^0 photoproduction from the proton as a function of t.

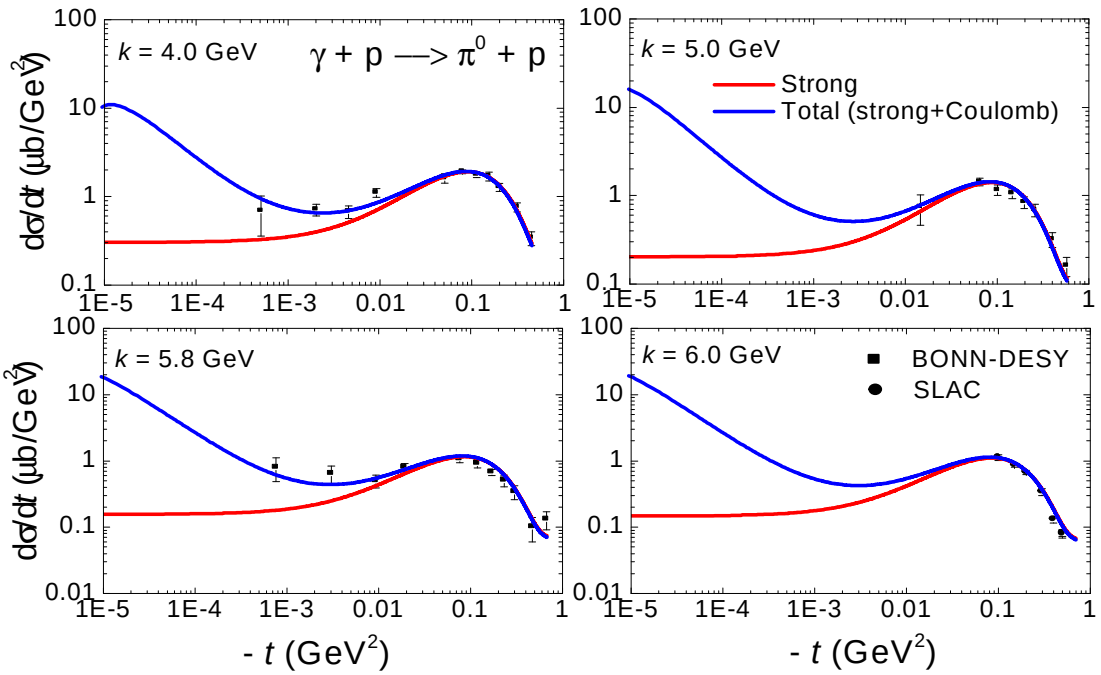

Figure 2: Differential cross section for π^0 photoproduction from the proton as a function of t. The notation is the same as in figure 1.

3 INCOHERENT π^0 PHOTOPRODUCTION FROM COMPLEX NUCLEI

This section aims at the description of the cascade calculations for incoherent π^0 photoproduction from complex nuclei. The calculations are suitable for light as well as heavy nuclei and can be applied for single pion photoproduction mechanisms within 4.0 to 6.0 GeV.

3.1 The cascade approach

The intranuclear cascade approach consists of a semi-classical transport calculation that describes the dynamics of a nuclear reaction via a time-dependent multicollisional Monte Carlo algorithm. The basic idea of the cascade model is that the active particles (particles that have kinetic energies above the Fermi energy) perform binary scatterings with the remaining nucleons during a time interval much lower than the collisional time between a pair of inactive particles (particles with kinetic energy below the Fermi level). The model can be applied for hadron and photon induced nuclear reactions, as far as we can neglect the effect of other nucleons during the first interaction mechanism. For high energy incoherent photoproduction processes, the photon is supposed to interact with a single nucleon and the rest of the nuclear wave function can be safely neglected. The two outgoing particles that come from the photoproduction vertex (the struck nucleon and the π^0 meson) are strongly susceptible to interact with the other nucleons, with high probability of producing additional mesons via Final State Interactions. These two trajectories can be treated semi-classically and are interpreted as two correlated branchings of the intranuclear cascade process. The amount of absorption of the primary π^0 photoproduction flux depends very critically on the photoproduction mechanism itself and also on the dynamics of the excited nuclear system. Such

complicated process is generally treated using event generators that account for the meson multiplicities and gross features of physical observables, such as the multiplicities of nucleons that are being emitted by the nucleus. This statistical approach is a convenient tool for the description of the general behavior of the nuclei, since it can be constructed and sometimes adjusted to reproduce the bulk properties of a high energy nuclear reaction. For the PrimEx Collaboration, however, the details of the multiple scatterings between the produced pions and the bound nucleons are of extreme relevance, since we need accurate information of the amount of energy loss and the contribution of secondary scatterings at forward angles. For this reason, an extended version of the MCMC cascade has been recently developed for the specific description of the incoherent π^0 photoproduction from Carbon and Lead at extreme forward angles. The flow diagram depicted in figure 3 shows the basic features and important modules of the cascade model.

The description of each module of the cascade model - which is certainly not the purpose of the present analysis - can be found elsewhere[18]. In the following sections, I will briefly describe some of the important modules and MCMC features for the specific case of the PrimEx experiment.

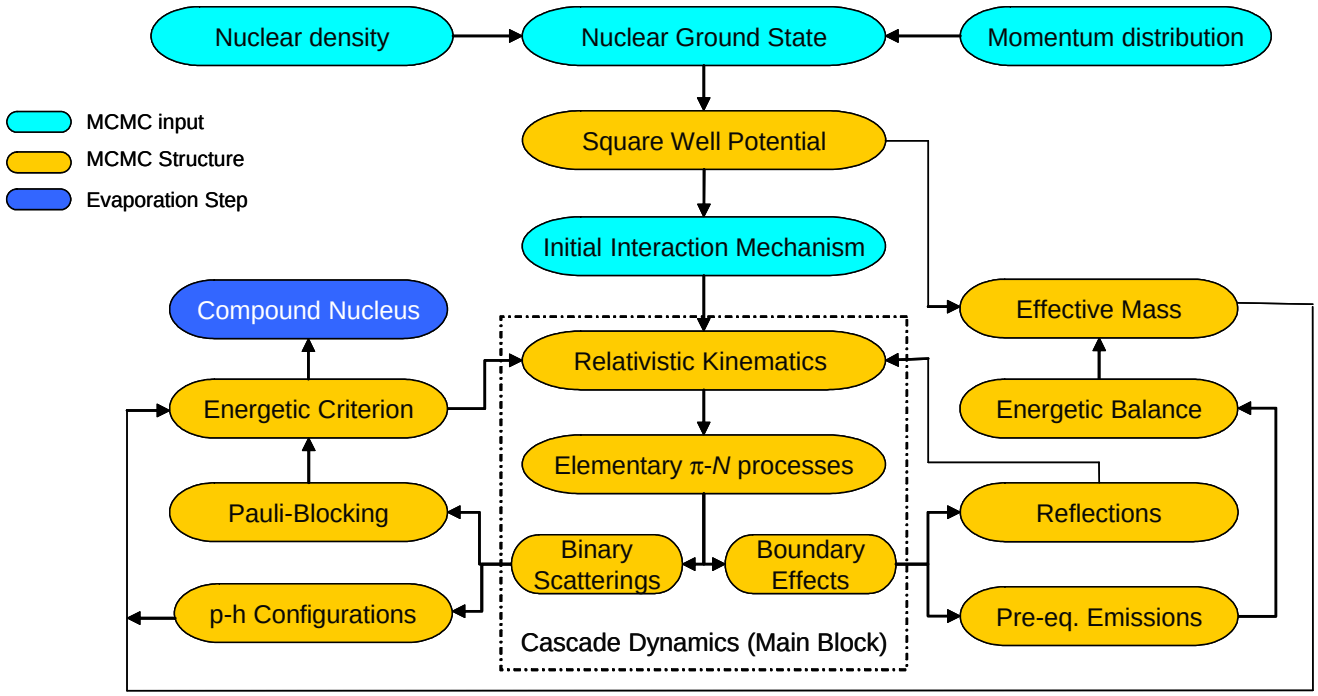

Figure 3: Flow diagram of the cascade model. The modules in light blue are associated with the physical inputs that feed the cascade model, while the orange modules represent the MCMC structure itself. The evaporation module (dark blue) is completely non-relevant in the present analysis and is presented only for the sake of completeness.

3.2 Nuclear ground state

3.2.1 Nuclear density

The positions of the bound nucleons in the Monte Carlo are distributed using the nuclear densities appropriate for light and heavy nuclei. For light nuclei, such as Carbon, we have adopted the shell-model distribution of ref.[19]:

$$N(r) = \frac{4}{\left(a_0\sqrt{\pi}\right)^3}\left(1+\frac{\delta r^2}{a_0^2}\right)\exp\left(\frac{-r^2}{a_0^2}\right), \tag{13}$$

where $a_0 = 1.65$ fm and $\delta = \frac{1}{6}(A-4)$. For intermediate and heavy nuclei, we have used a Woods-Saxon distribution given by[19]:

$$N(r) = \frac{N_0}{\exp\left[\frac{(r-c)}{z_1}\right]+1}, \tag{14}$$

where $c = 1.12A^{1/3}$ and $z_1 = 0.545$ fm, with $A = 4\pi\int N(r)r^2dr$. The nuclear densities for Carbon and Lead are shown in figure 4.

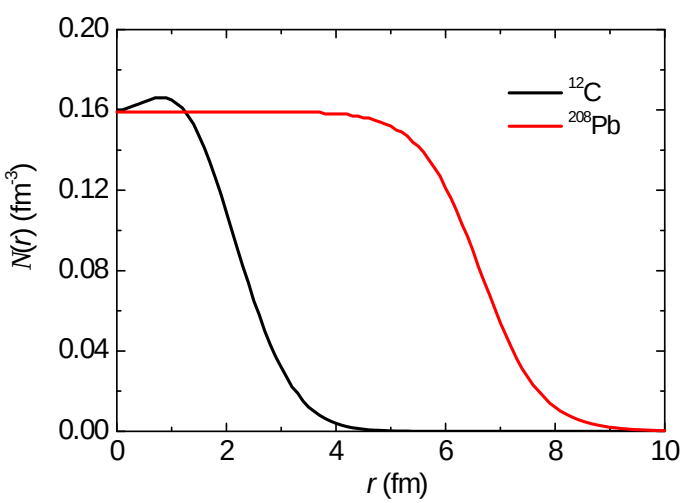

Figure 4: Normalized nuclear densities for Carbon (black) and Lead (red).

3.2.2 Momentum distribution of the bound nucleons

Another important physical constraint to build-up a realistic nuclear ground state is the momentum distribution (MD) of the bound nucleons. Since we are specifically concerned with high precision relativistic kinematics, we have to take into account the initial state of the struck nucleon very accurately. Furthermore, the Pauli-blocking mechanism plays an essential role for low t and small differences in the parameterizations of the MD´s affect drastically the shape of the cross sections at small angles. The PrimEx targets (C and Pb) have very distinct nuclear structures and the shapes of the NI cross sections should reflect these peculiarities. For this reason, two different MD were used in our calculations: one suitable for heavy nuclei, and another one specifically devoted for Carbon.

Momentum distribution for intermediate and heavy nuclei: The Fermi gas model is known to work reasonably well for nuclei with $A \gtrsim 100$, since the infinite nuclear matter approximation also holds with reasonable precision within this mass domain. For this reason, we can safely use the Fermi gas model for the case of Lead. In this model, the MD of the bound nucleons corresponds to a uniform distribution in a sphere in the momentum space:

$$W_F(p_N)d^3p_N = \frac{3}{4\pi}\frac{p_N^2}{p_F^3}dp_N \sin(\theta_p)d\theta_p d\varphi_p, \tag{15}$$

where p_F is the Fermi momentum and θ_p and φ_p the angular variables that define the direction of the 3-momentum of the nucleon $\mathbf{p}_N$. The Fermi momentum is calculated assuming that all nucleons are on-shell, $p_F = \sqrt{\varepsilon_F(\varepsilon_F + 2m_N^*)}$, where m_N^* is the nucleon effective mass with the Fermi energy

being given as a function of the nuclear volume $\Omega = \frac{4}{3}\pi r_0^3 A$ using the known formula:

$$\varepsilon_F^p = \frac{1}{2m_N^*}\left(3\pi^2\right)^{\frac{2}{3}}\left(\frac{Z}{\Omega}\right)^{\frac{2}{3}} \text{ and} \tag{16}$$

$$\varepsilon_F^n = \frac{1}{2m_N^*}\left(3\pi^2\right)^{\frac{2}{3}}\left(\frac{A-Z}{\Omega}\right)^{\frac{2}{3}}. \tag{17}$$

Momentum distribution for Carbon: Carbon is one of the most well studied nuclei of the periodic table and presents some peculiarities typical of small systems. The momentum distribution of the bound nucleons can be investigated using one-nucleon removal experiments, such as the quasi-elastic $(e, e\prime p)$ reaction. The missing energy E_m and missing momentum $\mathbf{p}_m$ can be written in the form:

$$\mathbf{p}_m = \mathbf{p}'_N - \mathbf{q}, \tag{18}$$

$$E_m = \omega - T_p - T_{A-1}, \tag{19}$$

where $\mathbf{p}'_N$ and T_p are the momentum and kinetic energy of the outgoing proton and T_{A-1} the kinetic energy of the residual nucleus. ω and $\mathbf{q}$ represent the energy and momentum transfer of the virtual photon. In PWIA, the fivefold differential $(e, e\prime p)$ cross section can be factorized in the form:

$$\sigma_{ee'p} = \frac{d^5\sigma}{d\Omega_e d\Omega_p dE_p} = K\sigma_{ep}\left|\phi_\alpha(\mathbf{p}_m)\right|^2, \tag{20}$$

where $K = \mathbf{p}'_N E_p$, σ_{ep} is the off-shell electron-proton scattering cross section [20], and $\phi_\alpha(\mathbf{p}_m)$ is the wave function in momentum space of the quantum state α, which can be approximated by a

single-particle bound-state wave function. The factorization presented in (20) does not hold if we take into account the distortion effects of the incident electron and outgoing proton and electron. However, one can still define the reduced cross section $\rho_{ee'p}(\mathbf{p}_m)$ by the ratio between the measured cross section and the electron-proton cross section:

$$\rho_{ee'p}(\mathbf{p}_m) = \frac{\sigma_{ee'p}}{K\sigma_{ep}}. \tag{21}$$

So, by measuring $\sigma_{ee'p}$, we can calculate the distorted momentum distribution $\rho_{ee'p}(\mathbf{p}_m)$, which in PWIA is the squared Fourier transform of the radial wave function.

Obviously that the distortion effects caused by the Final State Interactions of the emitted proton and electron, as well as the distortion effects on the wave function of the incident electron depend very critically on the reaction mechanism. These distortions do not permit a model independent result for the true momentum distribution of Carbon, which is the main focus of the present analysis. The true MD is the undistorted spectral function integrated in missing energies and is not achievable by proton knock-out experiments. For this reason, we have adopted the Plane Wave Impulse Approximation (PWIA) of ref.[21] for the momentum distributions of the s and $p-$shells as the reference input for the cascade calculation (see figure 5). A complete review of the global proton knock-out data of ^{12}C can be found in ref.[21] and references therein.

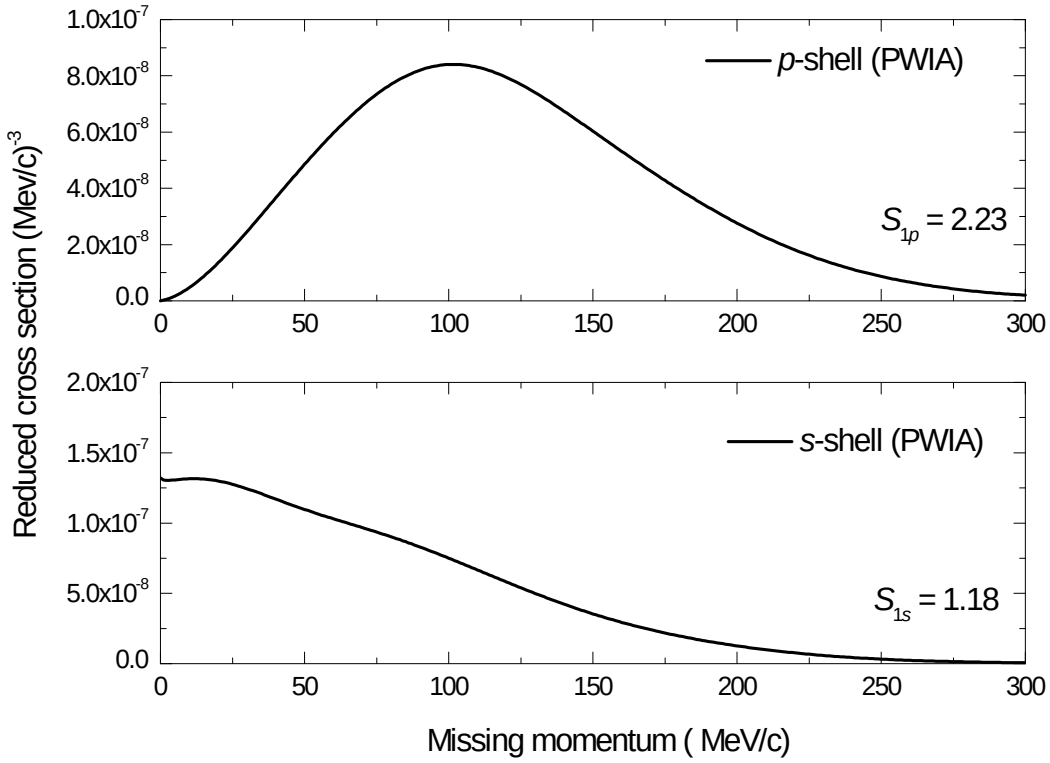

Figure 5: Reduced cross sections (momentum distributions) in PWIA for the s (bottom) and $p-$shells (top) of ^{12}C. The corresponding spectroscopic factors were taken from ref.[21].

In fact - complementary with the use of the PWIA for the MD - we have also run the cascade with several sets of parameterization based on the existing $^{12}\mathrm{C}(e, e\prime p)^{11}\mathrm{B}$ data. Such analysis propitiated the investigation of the sensitivity of the cascade model with a given parameterization, keeping the PWIA as the reference value. Table 1 summarizes the world data used in the calculations.

	Dataset	$\Delta E_m(MeV)$	$T_p(MeV)$	Kinematics	$Q^2(GeV/c)^2$
$1-p$ knock-out	Saclay 76[22]	$15-22$	87	perpendicular	0.16
"	Saclay 82[23]	$15-22$	99	parallel	$0.09-0.32$
"	Saclay 82[23]	$15-22$	99	perpendicular	$0.09-0.32$
"	Tokyo 76[24]	$6-30$	159	perpendicular	0.29
"	NIKHEF 88[25]	G.S.	70	parallel	$0.02-0.26$
$1-s$ knock-out	Saclay 76[22]	$30-50$	87	perpendicular	0.16
"	Tokyo 76[24]	$21-66$	136	perpendicular	0.29
"	NIKHEF 88[25]	$30-39$	70	parallel	$0.02-0.26$

Table 1: Proton knock-out data used in the present analysis. Details in the text.

The momentum distributions associated with the data from Table 1 were fitted separately and were incorporated as alternative inputs for the cascade model. The results of the NI cross sections using these empirical MD parameterizations, as well as the sensitivity of the model with respect to these inputs will be presented in another section. The fitted MD's with its respective data are shown in figures 6 to 9 ($p-$shell) and 10 to 12 ($s-$shell).

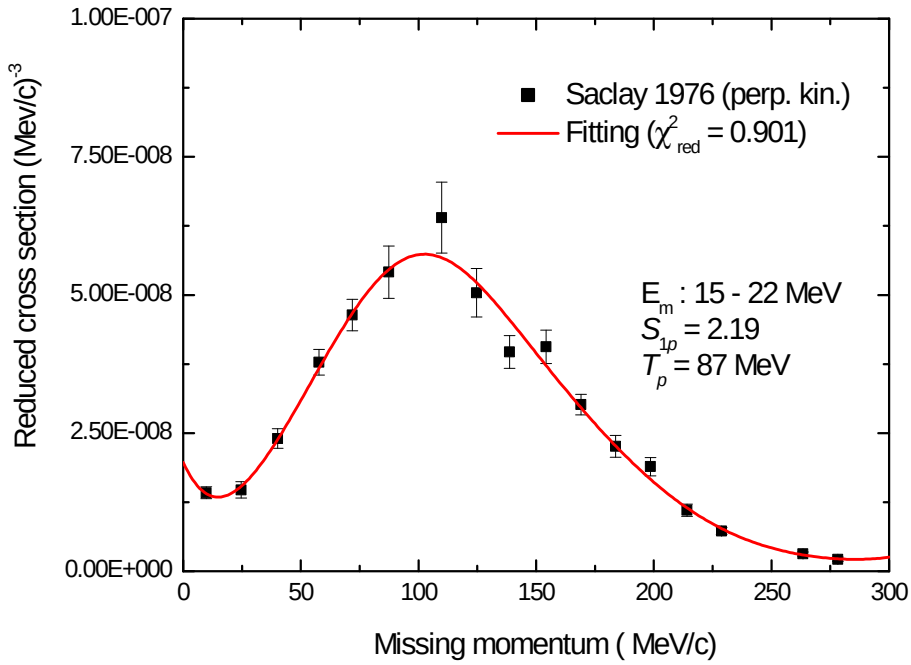

Figure 6: $1-p$ proton knock out. The data points are from ref.[22], while the red line is our fitting.

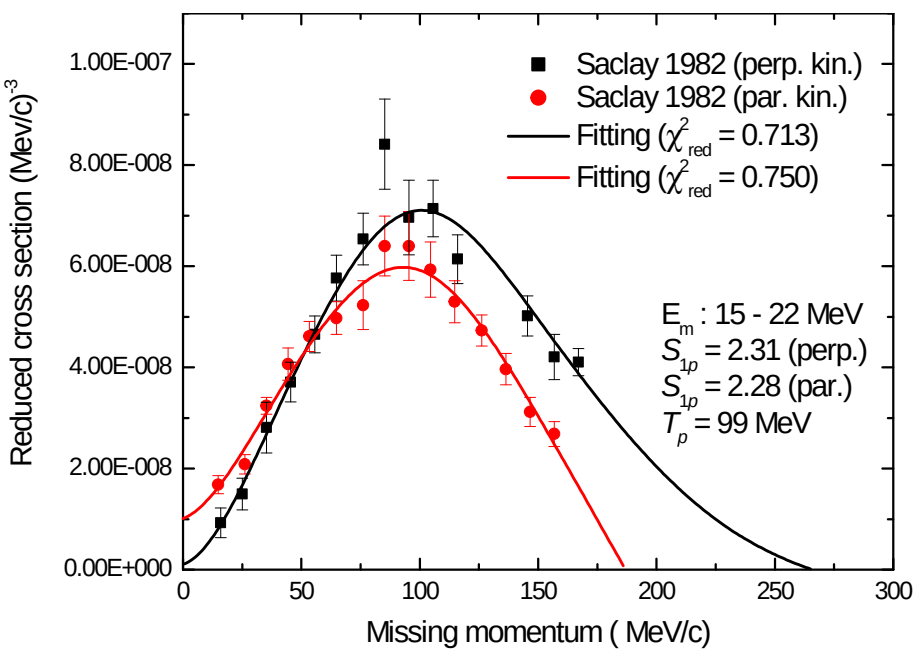

Figure 7: $1-p$ proton knock out. The data points are from ref.[23] and the red and black lines are the fittings for parallel and perpendicular kinematics, respectively.

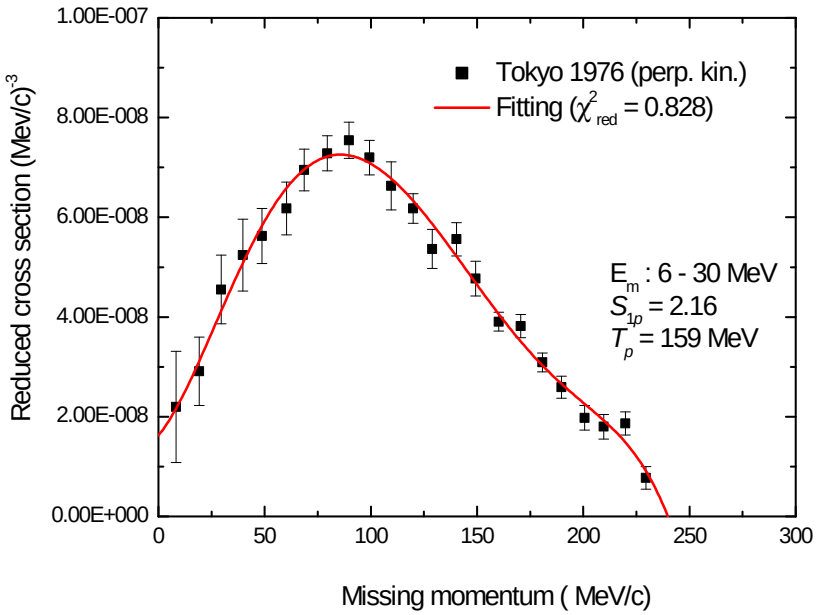

Figure 8: $1-p$ proton knock out. The data points are from ref.[24] and the red line represents our fitting.

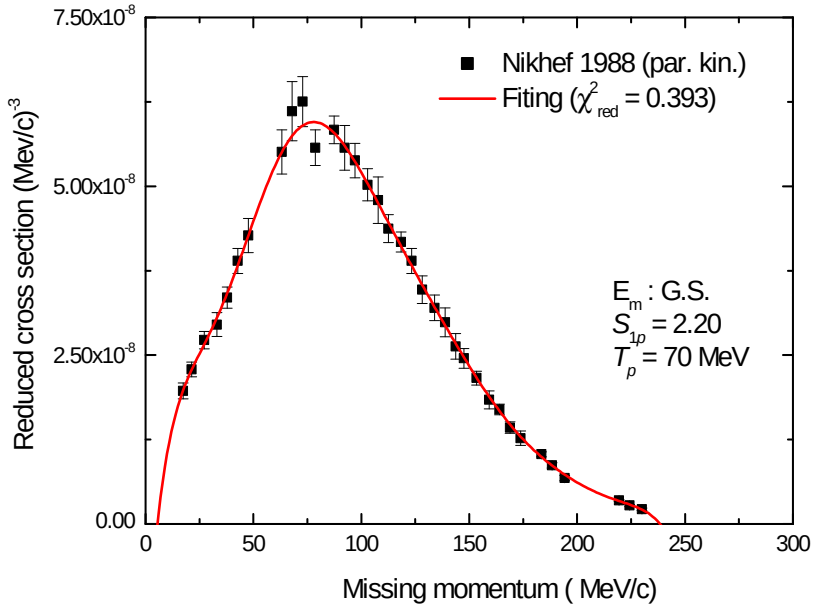

Figure 9: $1-p$ proton knock out. The data points are from ref.[25] and the red line represents our fitting.

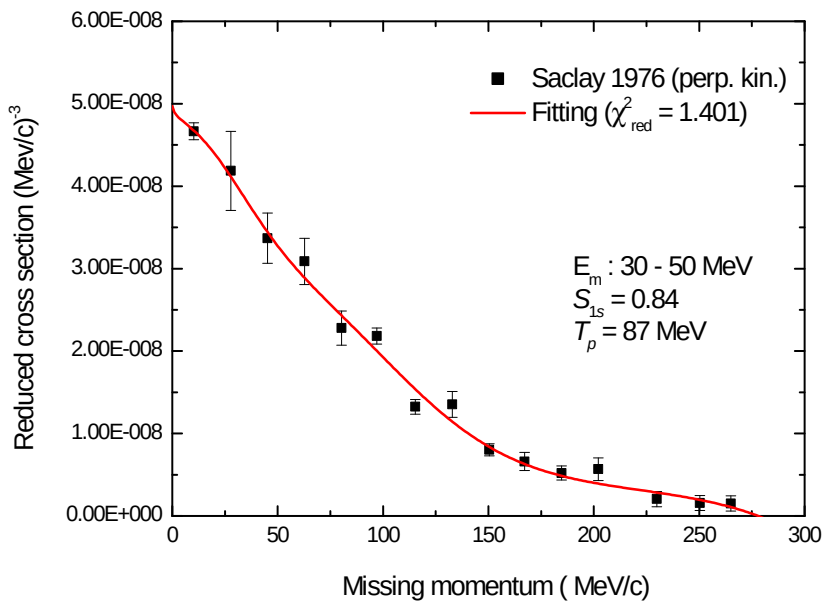

Figure 10: $1-s$ proton knock out. The data points are from ref.[22] and the red line represents our fitting.

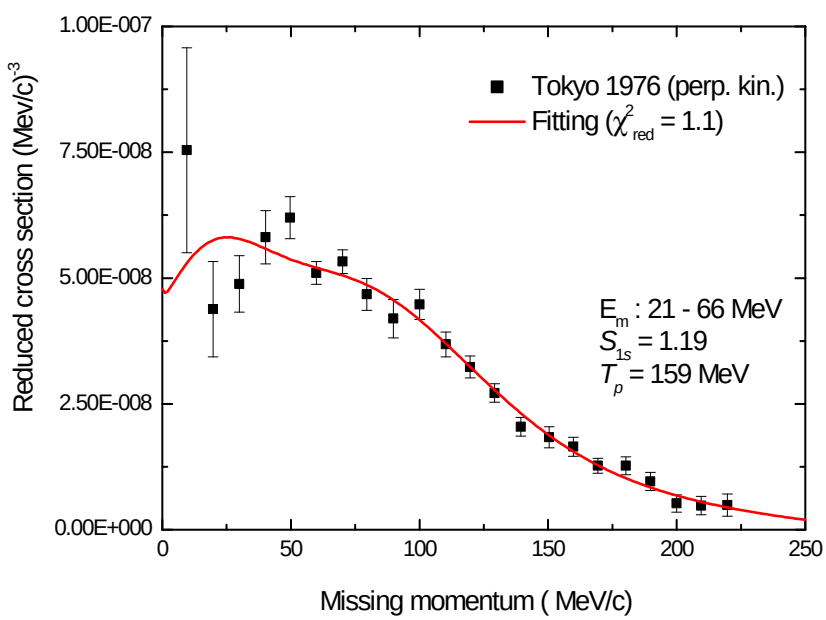

Figure 11: $1-s$ proton knock out. The data points are from ref.[24] and the red line represents our fitting.

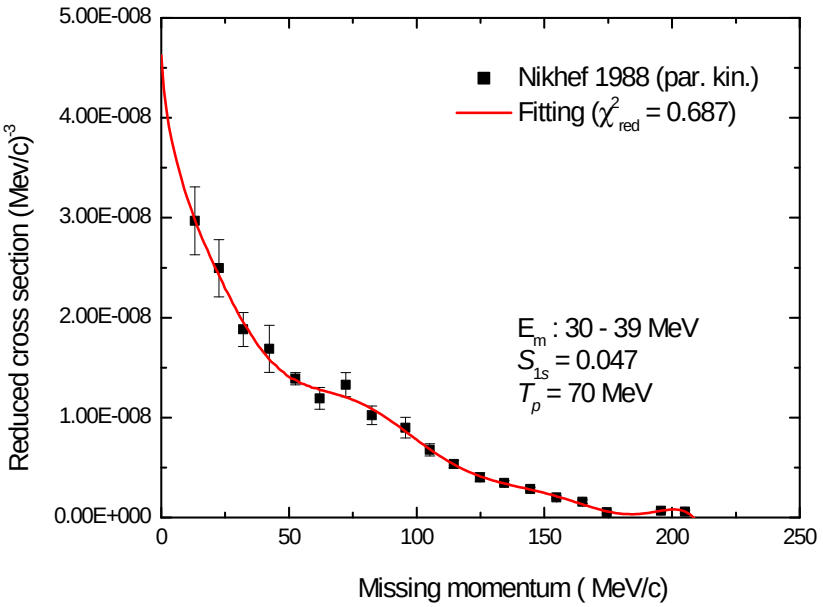

Figure 12: $1-s$ proton knock out. The data points are from ref.[25] and the red line represents our fitting.

3.3 Shadowing effects in high energy photo-nucleus interactions

The direct coupling of high energy photons with vector mesons propitiates a phenomenological analogy between photon and hadron induced nuclear reactions. The main hypothesis of the VMD model is that the physical photon state can be decomposed into a bare and hadronic component, where the former is not expected to interact with hadrons. So, the photon state is assumed to be given by[26]:

$$|\gamma\rangle \cong \sqrt{Z_3}\,|\gamma_B\rangle + \sqrt{\alpha}\,|h\rangle\,, \tag{22}$$

where the factor Z_3 is introduced for the normalization of $|\gamma\rangle$. One important constraint of the theory is that both $|\gamma_B\rangle$ and $|h\rangle$ have the same quantum numbers $\left(J^{PC} = 1^{--}\right)$ and the same 3-momentum of the physical photon k. The assumption that the hadronic state $|h\rangle$ is solely attributed to the vector mesons ρ, ω and ϕ is one of the main restrictions of the VMD model and is also employed in the present analysis. Considering only the low-mass components of the photon and a narrow resonance state, we may write $\sqrt{\alpha}\,|h\rangle$ as a superposition of vector meson states:

$$\sqrt{\alpha}\,|h_s\rangle_{res} = \sum_V \frac{e}{f_V}\,|V\rangle\,, \tag{23}$$

where $\frac{e}{f_V}$ is our choice of normalization for real photons[26], with the label s indicating that such approximation is valid only for low mass constituents. For higher mass components, however, the interaction of the vector mesons with hadrons is typically *short-ranged* and the hadronic photon behaves similarly as a bare photon without substantial shadowing. Assuming that the bare photon does not interact (VMD), we may connect the scattering amplitudes for high energy $\gamma N \to X$ processes to analogous amplitudes of vector meson scattering $VN \to X$ using the S matrix:

$$\langle X|\, S\, |\gamma N\rangle = \sum_V \frac{e}{f_V} \langle X|\, S\, |VN\rangle\,. \tag{24}$$

Employing the diagonal approximation and using (24), we may write the total photoabsorption cross section in hadrons $\sigma_{\gamma N}$ due to vector mesons in the form:

$$\sigma_{\gamma N} = \sum_V \frac{e^2}{f_V^2} \sigma_{VN}, \tag{25}$$

where σ_{VN} is the total VN cross section. Taking the coupling constants and the VMD model II from ref.[26] ([4]), we have:

$$\sigma_{\rho N} = \sigma_{\omega N} = 19.1 \left(1 + \frac{0.766}{\sqrt{p(GeV/c)}}\right) \text{ mb and} \tag{26}$$

$$\sigma_{\phi N} = 12 \text{ mb.} \tag{27}$$

So, inserting eqs.(26 - 27) into (25), we find for $k = 5.2$ GeV:

$$\sigma_{\gamma N}^{\rho} = 84.7\ \mu\text{b};\ \sigma_{\gamma N}^{\omega} = 7.9\ \mu\text{b};\ \sigma_{\gamma N}^{\phi} = 4.8\ \mu\text{b}, \tag{28}$$

with a non-shadowed (NS) component of $\sigma_{\gamma N}^{NS} = 24.5\ \mu$b, yielding a total cross section of $\sigma_{\gamma N}^{Total} = 121.8\ \mu$b. This value should be compared with the experimental results of $\sigma_{\gamma p}^{Total} = 116 \pm 17\ \mu$b found in the energy interval $3.5 \leq k \leq 5.4$ GeV[27] and $\sigma_{\gamma p}^{Total} = 126 \pm 17\ \mu$b found at 7.5 GeV[28]([5]).

[4] Table XXXV of ref.[26] summarizes the values of the coupling constants and the features of the VMD model used in the present analysis.

[5] No distinction is made between the proton and neutron amplitudes in this approach, such that $\sigma_{\gamma N}^{Total} = \sigma_{\gamma p}^{Total} = \sigma_{\gamma n}^{Total}$. The Coulomb term affects only the NS contribution, but is neglected for the calculation of the NI cross section. For details see section 2.

Another important step for the evaluation of shadowing effects for photo-nucleus interactions is the concept of *formation time*, which is the time interval that the physical photon is *momentarily in a vector meson state*. The physical photon is always making transitions back and forth between a bare photon and hadronic states, keeping the steady state of eq.(22). Shadowing effects are expected to take place if the *formation time* is long enough to allow the virtual hadrons to undergo collisions deep in the nuclei as if they were real hadrons. We can estimate the *formation time* using the uncertainty principle:

$$t_f \sim \left| \frac{1}{k - \sqrt{k^2 + m_V^2}} \right|, \tag{29}$$

where m_V is the mass of the vector meson. Obviously that this crude estimate gives only the order of magnitude of t_f, making it necessary further investigations of the quantitative results presented later in this section ([6]). The vector meson mass m_V can be calculated using the ρ meson as a reference, since it contributes to approximately 70% of $\sigma_{\gamma N}^{Total}$, and a lorentzian distribution:

$$W(m_V) = \frac{1}{2\pi} \frac{\Gamma_\rho}{(m_V - m_\rho)^2 + \left(\frac{\Gamma_\rho}{2}\right)^2}, \tag{30}$$

with $m_\rho = 769.3$ MeV and $\Gamma_\rho = 150.2$ MeV. The corresponding values of t_f are then distributed combining eqs. (29 - 30) and using M.C. techniques. For instance, taking the central value $m_V = m_\rho$, we found $t_f^0 \sim 3.5$ fm/c for 5.2 GeV, which is associated with a *formation distance* of ~ 3.5 fm, considering that the virtual particle is traveling almost at the speed of light. From a direct inspection of eq.(29), we note that t_f increases with higher photon energies and lower vector meson masses,

[6]The VMD model used in this analysis, as well as the estimated value of t_f, provide additional theoretical background for the qualitative interpretation of the shadowing effects during non-diffractive π^0 photoproduction from nuclei. The quantitative results obtained in this section are not supposed to reproduce the PrimEx data, but to be certainly superseded by the accurate results from measurements from Carbon and Lead. Additional discussion on this subject will be presented in the conclusions.

showing qualitatively that shadowing effects are much less relevant for higher mass constituents of the photon. The energy dependence of t_f affects the photon ability to interact with hadrons. The higher is the photon energy, the stronger is its attenuation deep in the nuclei. The relationship between ct_f and the size of the nucleus also originates a much steeper decrease of the photoabsorption cross section for heavier nuclei at higher energies, in comparison with light systems that tend to reach an asymptotic value for much lower energies ~ 6 GeV.

The calculation of the shadowing effect is carried out taking advantage of the MCMC cascade model in a straightforward approach. The nuclear photoabsorption cross section is expected to be proportional to the single nucleon cross section as follows:

$$\sigma_{\gamma A}^{abs} = A_{eff}^{abs} \sigma_{\gamma N}^{Total}, \tag{31}$$

where the ratio $\frac{A_{eff}^{abs}}{A}$ gives the amount of shadowing and is equal to unit for a pure electromagnetic interaction (non-shadowed component). The label *abs* is introduced to indicate that we are considering the total photo-nucleus cross section at this point. Later on this note I will address the A_{eff} factor for π^0 photoproduction specifically.

The factor A_{eff}^{abs} can be calculated gathering information of the nuclear transparency to vector mesons. In this approach, we can calculate A_{eff}^{abs} using the separation of (28) and the additional *NS* contribution:

$$A_{eff}^{abs} = \frac{\sigma_{\gamma N}^{NS}}{\sigma_{\gamma N}^{Total}} A + 4\pi \left[\frac{\sigma_{\gamma N}^{\rho} + \sigma_{\gamma N}^{\omega}}{\sigma_{\gamma N}^{Total}} \int \mathrm{T}_{\rho,\omega}(r) N(r) r^2 dr + \frac{\sigma_{\gamma N}^{\phi}}{\sigma_{\gamma N}^{Total}} \int \mathrm{T}_{\phi}(r) N(r) r^2 dr \right], \tag{32}$$

where $\mathrm{T}_V(r)$ is the transparency for the respective vector meson ($V \equiv \rho, \omega, \phi$). Since in our model $\sigma_{\rho N} = \sigma_{\omega N}$, we have $\mathrm{T}_{\rho}(r) = \mathrm{T}_{\omega}(r) = \mathrm{T}_{\rho,\omega}(r)$. Obviously that for a non-shadowed photoabsorption,

we have $T_V(r) = 1$ and eq.(32) gives $A_{eff}^{abs} = A$. The nuclear transparency of vector mesons is calculated as a function of the radial distance considering that vector mesons are coupled with photons with impact parameters uniformly distributed in the area of a disc perpendicular to the photon direction (z axis). For each cascade run, the vector meson mass m_V and *formation time* t_f are distributed according with eqs.(29 - 30), conserving the 3-momentum of the system. The *formation time* t_f starts immediately after the vector meson and the struck nucleon reach their minimal relative distance and the primary VN collisions are collected. This analysis provides the information about the respective nuclear transparencies both in the incident ($z < 0$) and opposite ($z > 0$) sides of the nucleus. The transparencies for Carbon and Lead for the three hadronic constituents of the photon are shown in figures 13 and 14, respectively.

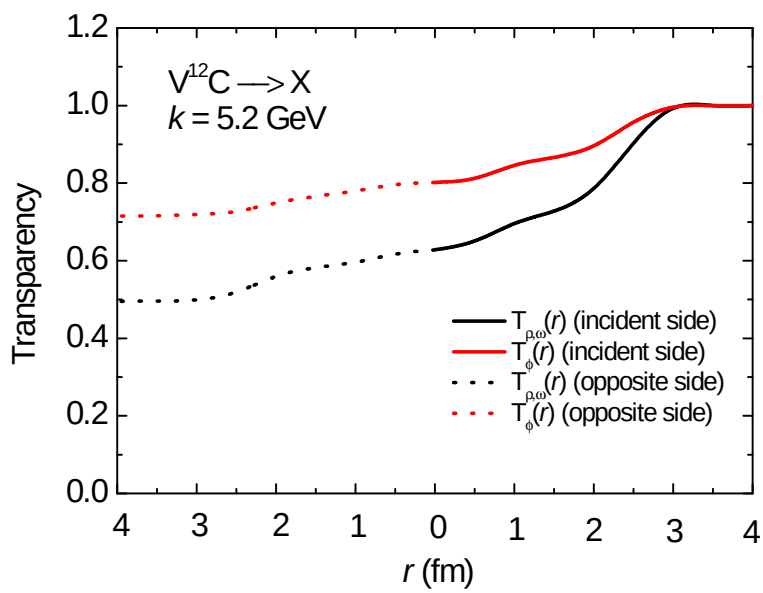

Figure 13: Nuclear transparency of ^{12}C to vector mesons calculated via the MCMC cascade model. Details in the text.

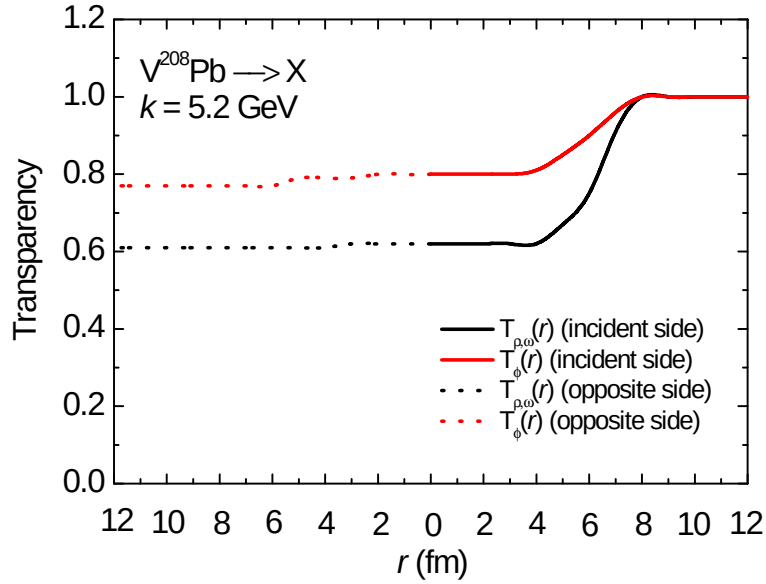

Figure 14: Nuclear transparency of ^{208}Pb to vector mesons calculated via the MCMC cascade model. Details in the text.

So, including the MCMC results for $T_V(r)$ in eq.(32), one immediately obtains: $\frac{A^{abs}_{eff}}{A} = 0.76$ for Carbon, and $\frac{A^{abs}_{eff}}{A} = 0.75$ for Lead. It is interesting to make salient that both factors are compatible, even though one should expect a much higher attenuation for the case of Lead. However, the nuclear transparency also depends on the *formation time* t_f, reaching an asymptotic value after the hadronic component is switched off. Such mechanism is very clear for the case of Lead (Figure 14), which consists of a huge system where the interactions of the hadronic constituents with the nucleons are unlikely to occur after a typical formation distance. For the case of Carbon, on the other hand, the nuclear transparency is still decreasing deep in the nuclei, since the formation distance is compatible with the nucleus size at 5.2 GeV and the vector mesons are expected to probe the whole nucleus. For higher energies, however, the attenuation in Lead should be much stronger and the ratio $\frac{A^{abs}_{eff}}{A}$ much lower, but at 5.2 GeV it is almost the same as for Carbon([7]).

[7]The values of A^{abs}_{eff} for Carbon and Lead obtained with this simple approach are reasonably consistent with the

3.4 Pauli-blocking in π^0 photoproduction from complex nuclei

The accurate determination of the inelastic background in the PrimEx experiment is one of the most important challenges of the available nuclear models. The precise data from PrimEx demand a state-of-the-art approach for the understanding of the hadronic inelastic background, since strong correlations are expected between some of the fitted parameters, such as the $\pi^0 \to \gamma\gamma$ decay width and the Primakoff $-$ nuclear coherent (NC) phase shift. Also, the magnitude of the NC and NI cross sections are strongly correlated and energy dependent, making it necessary a clear interpretation of the Pauli-blocking mechanism at small angles. The Pauli-suppression factor can be calculated analytically considering the Fermi gas model with the infinite nuclear matter approximation or an independent particle model with Harmonic Oscillator (HO) wave functions. The former calculation is expected to work properly for heavy nuclei, such as Lead, while the later is useful for the description of finite nuclei effects in light and double magic nuclei, such as ^{16}O. A detailed review about neutral pion photoproduction from complex nuclei up to 900 MeV and the Pauli-blocking suppression factors for heavy and light nuclei can be found in ref.[29] and references therein. In this approach, the Pauli-suppression factor for heavy nuclei is given by:

$$\begin{aligned} 1 - G(q) &= \frac{3}{4}\left(\frac{q}{p_F}\right) - \frac{1}{16}\left(\frac{q}{p_F}\right)^3 \text{ for } q < 2p_F \text{ and} \\ &= 1 \text{ for } q > 2p_F, \end{aligned} \tag{33}$$

where p_F is the Fermi momentum with $q \sim k\theta$ representing the 3-momentum transfer. For light nuclei, the following expression was obtained:

values reported on ref. [26] (see fig. 202), even though they provide only crude estimates for the case of PrimEx.

$$1 - G(q) = 1 - \left[1 + \left(\frac{q}{2\alpha}\right)^4\right] \exp\left(\frac{-q^2}{2\alpha^2}\right), \tag{34}$$

where $\alpha^2 = \frac{15}{4R^2} \simeq 0.019\ (GeV/c)^2$.

The MCMC model, on the other hand, consists of an appropriate tool for the accurate determination of the Pauli-blocking suppression factor. Eqs. (33) and (34) were derived using closure approximation without any specification about the photoproduction operator. The MCMC model also requires closure, since the NI amplitude for π^0 photoproduction from the nucleus is obtained as an incoherent sum of single nucleon amplitudes, but it still possible to include the dynamical information for the elementary photoproduction during the evaluation of the Pauli-suppression factor. This powerful Monte Carlo method provides a more accurate calculation of the Pauli-blocking, since it accounts for the underlying dynamics of the photoproduction mechanism. For the case of heavy nuclei, such as Lead, one should expect only small differences between eq.(33) and the MCMC model, since both methods are based on the Fermi gas. These differences arise from the nucleon effective masses (binding effect), the neutron-proton asymmetry in heavy nuclei, and the relativistic kinematics for the struck nucleon used in the MCMC model, besides the dynamics of the π^0 photoproduction previously mentioned. For the specific case of Carbon, one should expect significant differences between the MCMC model and the calculations presented in ref.[29] due to the inclusion of realistic M.D. of the bound nucleons based on the $1-s$ and $1-p$ proton knock-out data. The Pauli-blocking factor in the MCMC model − herein denoted f_{PB} ([8]) − is easily obtained by the ratio between Pauli-allowed and the total number of events, after distributing the π^0 production angle in the center of mass of the $s-$channel using eq.(8). So, the total cross section after

[8]For notation purposes we are using f_{PB} for the suppression factor calculated in the MCMC routine (for Carbon and Lead) and G for the analytical solutions presented in eqs.(33) and (34).

the inclusion of the Pauli-principle $\left(\frac{d\sigma}{d\Omega}\right)_A^{PB}$ can be written as:

$$\left(\frac{d\sigma}{d\Omega}\right)_A^{PB} = f_{PB}(k,\theta)\left(\frac{d\sigma}{d\Omega}\right)_A^{PWIA} = Af_{PB}(k,\theta)\left(\frac{d\sigma}{d\Omega}\right)_N . \tag{35}$$

Figure 15 shows the results of the Pauli-blocking factors as a function of polar angle ($\theta_{\pi^0} \sim \frac{q}{k}$) obtained via the MCMC model for ^{208}Pb (blue line) and using eq.(33) with the same Fermi momentum of $p_F = 279$ MeV/c (black line). Since eq.(33) was derived independently of the photoproduction dynamics, it is convenient to compare the prediction of the cascade model assuming an isotropic π^0 photoproduction in the center of mass of the $s-$channel (red line), where one easily verifies a very nice agreement between these approaches. It is clear that the Pauli-blocking factor depends upon the photoproduction mechanism, since the later is much more favorable for π^0 photoproduction at forward angles, enhancing the Pauli-blocking factor (less Pauli-suppression). The results for Carbon are shown in figure 16, where we have used a Fermi momentum of 221 MeV/c[30] for the cascade calculations. A remarkable shape difference between the MCMC predictions and the one obtained with eq. (34) is observed. It is worth-mentioning, however, that the H.O. potential used in ref.[29] is expected to work properly for nuclei with closed s and $p-$shells, such as the working example presented there for ^{16}O. In this model, the $p_{3/2}$ and $p_{1/2}$ states are degenerated (no spin-orbit coupling), propitiating an analytical expression for $G(k,\theta)$. However, for the PrimEx target ^{12}C, the spin-orbit term plays an essential role, making the H.O. approximation a crude estimate in comparison with the accurate M.D. used in the MCMC model (see previous section).

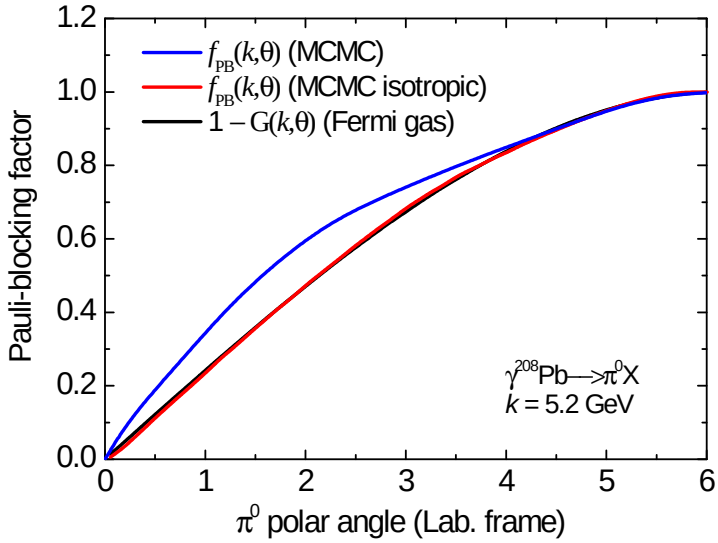

Figure 15: Pauli-blocking factor for π^0 photoproduction on ^{208}Pb. The blue line represents the MCMC model prediction taking into account the π^0 photoproduction parameterization of eq. (8), while the red line is the same result using an isotropic distribution of events. The result obtained with eq.(33) is shown by the black line.

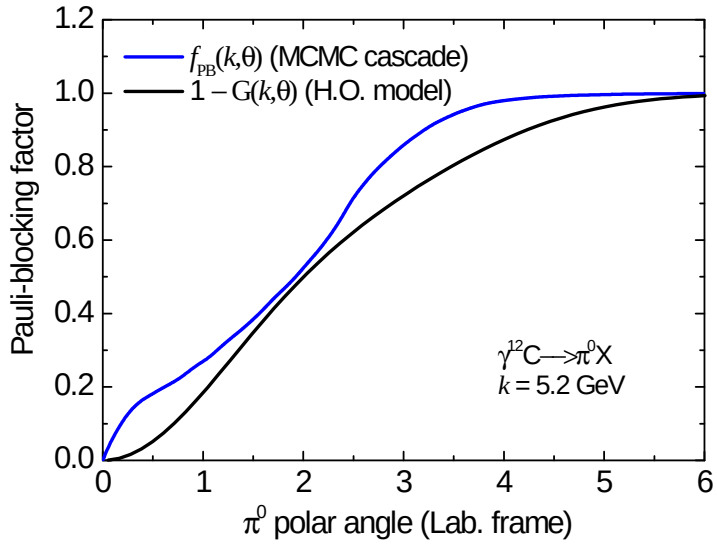

Figure 16: Pauli-blocking factor for π^0 photoproduction on ^{12}C calculated in the MCMC model (blue line) and using eq.(34) (black line).

3.5 π^0- nucleus final state interactions.

The calculation of the Final State Interactions (FSI) of the neutral pions with the nucleus consists of the main issue for the determination of the NI cross section. The huge amount of open channels requires a powerful tool, based on a sophisticated Monte Carlo algorithm, to address the dynamics of such complicated system. The main disadvantage of the Glauber model for the calculation of the absorption effects in π^0 photoproduction is that it does not account for the energy losses during secondary scatterings and also neglects the short range correlations for particles that undergo into collisions. These two approximations are expected to be quite reasonable if we consider $\pi^0 N$ scatterings in a high momentum transfer regime. For forward angle photoproduction, however, *soft* scatterings are more strongly Pauli-forbidden, affecting the NI cross section in shape and magnitude.

Table 2 presents the $\pi N \rightarrow X$ channels considered in the MCMC cascade. The entrance channels are given by binary collisions with one pion (π^0, π^+, π^-) and one nucleon (p, n). Collisions of the type $\pi N, \pi N^*, \pi\Delta, NN, NN^*$ and $N\Delta$ are taken into account, but collisions between pairs of pions are not considered due to a much lower pion density. There is a huge amount of important channels for the case of PrimEx, since a great number of additional neutral pions can be produced in secondary scatterings. In fact, multiple pion production dominates the total cross section within the PrimEx energy range. The energy dependence of the cross sections for the entrance channels $\pi^0 p$ and $\pi^0 n$ are presented in figures 17 and 18, respectively.

CHANNEL IN	π^0p	π^+p	π^-p	π^0n	π^+n	π^-n
CHANNEL OUT	pπ^0	pπ^+	pπ^-	nπ^0	nπ^+	nπ^-
	$\Delta(1232)^+$ (P_{33})	$\Delta(1232)^{++}$ (P_{33})	$\Delta(1232)^0$ (P_{33})	$\Delta(1232)^0$ (P_{33})	$\Delta(1232)^+$ (P_{33})	$\Delta(1232)^-$ (P_{33})
	$N(1520)^+$ (D_{13})		$N(1520)^0$ (D_{13})	$N(1520)^0$ (D_{13})	$N(1520)^+$ (D_{13})	
	$N(1680)^+$ (F_{15})		$N(1680)^0$ (F_{15})	$N(1680)^0$ (F_{15})	$N(1680)^+$ (F_{15})	
	$\Delta(1950)^+$ (F_{37})	$\Delta(1950)^{++}$ (F_{37})		$\Delta(1950)^0$ (F_{37})		$\Delta(1950)^-$ (F_{37})
	nπ^+		nπ^0	pπ^-	pπ^0	
	p2π^0	p$\pi^0\pi^+$	p$\pi^-\pi^0$	n2π^0	p$\pi^0\pi^+$	p$\pi^-\pi^0$
			n2π^0		p2π^0	
	p3π^0	p2$\pi^0\pi^+$	pπ^-2π^0	n3π^0	n2$\pi^0\pi^+$	pπ^-2π^0
	pπ^-2$\pi^0\pi^+$	p$\pi^-\pi^0$2π^+	p2$\pi^-\pi^0\pi^+$	nπ^-2$\pi^0\pi^+$	n$\pi^-\pi^0$2π^+	n2$\pi^-\pi^0\pi^+$
	n3$\pi^0\pi^+$	n2$\pi^0$2π^+	n$\pi^-\pi^0$2π^+	pπ^-3π^0	nπ^-2$\pi^0\pi^+$	n2π^-2π^0
	n$\pi^0\pi^+$	n2π^+	n$\pi^-\pi^+$	p$\pi^-\pi^0$	p$\pi^-\pi^+$	p2π^-
	p$\pi^-\pi^0\pi^+$	pπ^-2π^+	p2$\pi^-\pi^+$	n$\pi^-\pi^0\pi^+$	nπ^-2π^+	n2$\pi^-\pi^+$
	n$\pi^-\pi^0$2π^+	nπ^-3π^+	nπ^-2π^+	p2$\pi^-\pi^0\pi^+$	p2π^-2π^+	p3$\pi^-\pi^+$
	n2$\pi^0\pi^+$	nπ^0 2π^+	n$\pi^-\pi^0$ π^+	pπ^-2π^0	p$\pi^-\pi^0$ π^+	p2$\pi^-\pi^0$
			n3π^0		p3π^0	
	p2$\pi^-\pi^0$2π^+	p2π^-3π^+	p3π^-2π^+	n2$\pi^-\pi^0$ 2π^+	n2π^-3π^+	n3π^-2π^+
	n2$\pi^-\pi^0$3π^+	n2π^-4π^+	n3π^-3π^+	p3$\pi^-\pi^0$2π^+	p3π^-3π^+	p4π^-2π^+
	p2π^-2$\pi^0$2π^+	p2$\pi^-\pi^0$3π^+	p3$\pi^-\pi^0$2π^+	n2π^-2$\pi^0$2π^+	n2$\pi^-\pi^0$3π^+	n3$\pi^-\pi^0$2π^+
	p4π^0	p3$\pi^0\pi$+	pπ^-3π^0	n4π^0	n3$\pi^0\pi^+$	nπ^-3π^0
	pπ^-3$\pi^0\pi^+$	pπ^-2$\pi^0$2π^+	p2π^-2$\pi^0\pi^+$	nπ^-3$\pi^0\pi^+$	nπ^-2$\pi^0$2π^+	n2π^-2$\pi^0\pi^+$
	(+n)→pn	(+n)→pp	(+n)→nn	(+p)→np	(+p)→pp	(+p)→nn

Table 2: $\pi N \rightarrow X$ channels implemented in the MCMC cascade model. Details in the text.

The cross sections for the $\pi N \rightarrow X$ channels included in the MCMC model were obtained combining the properties of isospin invariance and time reversal of the strong interactions and the results for charged pions, usually determined by fitting the experimental data. This procedure allowed the inclusion of approximately 95% of the relevant channels within the PrimEx energy, where we have neglected production of vector mesons and strange particles.

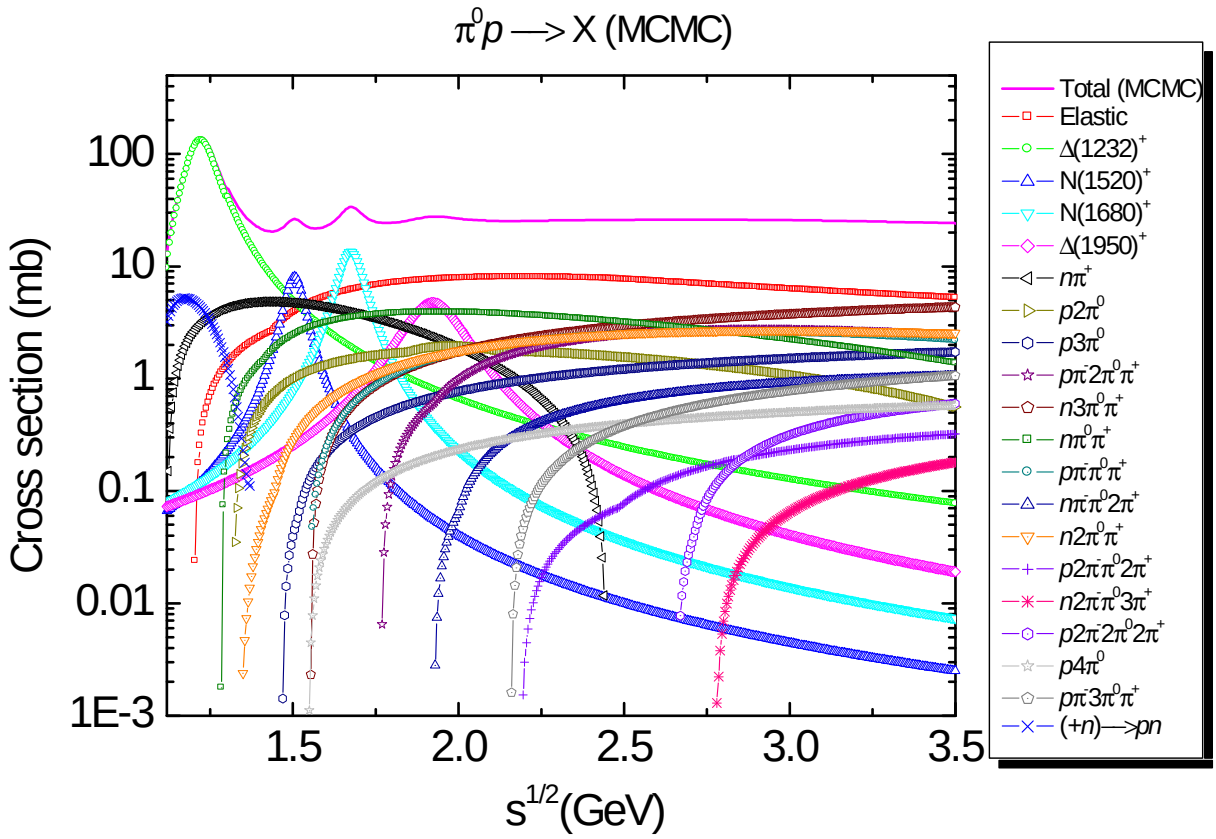

Figure 17: $\pi^0 p \longrightarrow X$ channels implemented in the MCMC model.

A typical entrance channel for a charged pion and its respective experimental data is presented in figure 19. The solid blue line represents our fitting, while the magenta line is the sum of all processes included in the MCMC model, indicating that almost all channels were accounted for. The missing channels refer to the production of vector mesons and strange particles and were not included into the cascade. However, for the calculation of the interaction probability, we considered the total πN cross section (blue line for the case of figure 19), instead of the evaluated total cross section in order to properly account for the pion transparency. The elastic channel is approximately 20 % of the total cross section for $k = 5.2$ GeV ($\sqrt{s} \approx 3.2$ GeV) and consists of the major contribution of

secondary scatterings within the PrimEx energy range. This specific channel needs special attention and will be described in more detail later.

The main focus of the present calculation is to provide a rigorous method for the determination of the NI contribution in the quasi-elastic hadronic background of the PrimEx data. Obviously that the current version of the cascade model is not intended to calculate the total π^0 background within 4.0 to 6.0 GeV, which is certainly not feasible considering the current status of the nuclear theory. The main reason for this limitation is attributed to the fact that only the single pion production channel is considered during the first photo-nucleus interaction (see previous section).

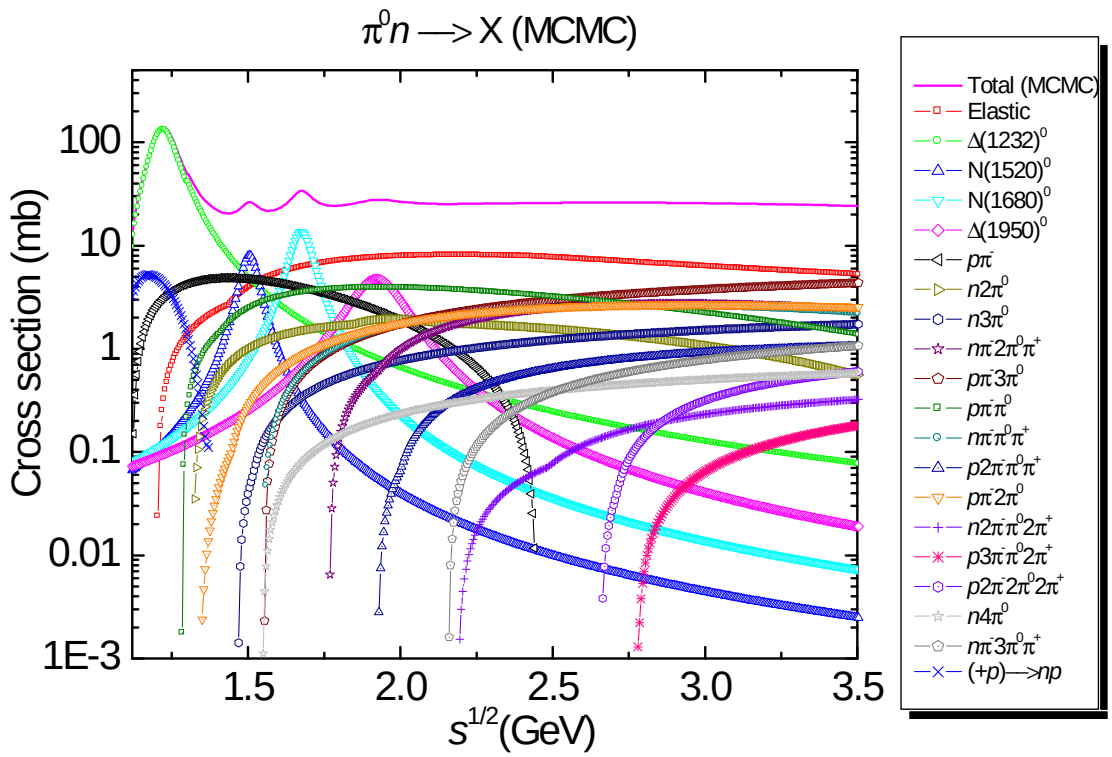

Figure 18: $\pi^0 n \rightarrow X$ channels implemented in the MCMC model.

This single meson photoproduction mechanism represents only a small fraction ($\sim$ 10%) of the total hadronic cross section [28] and, consequently, restricts our analysis to the quasi-elastic domain. So, the calculations and results that follow consider only a single π^0 photoproduction that subsequently interacts with the bound nucleons in accordance with the elementary processes depicted in figures 17 and 18 and in table 2. For this reason, a careful analysis of the π^0 production kinematics that might contribute in the quasi-elastic domain has to be carried out, showing that not only the single differential but also the double-differential π^0 production cross section $\left(\frac{d^2\sigma}{d\Omega dE_{\pi^0}}\right)$ has to be considered during the data analysis in order to access the neutral pion energy spectra.

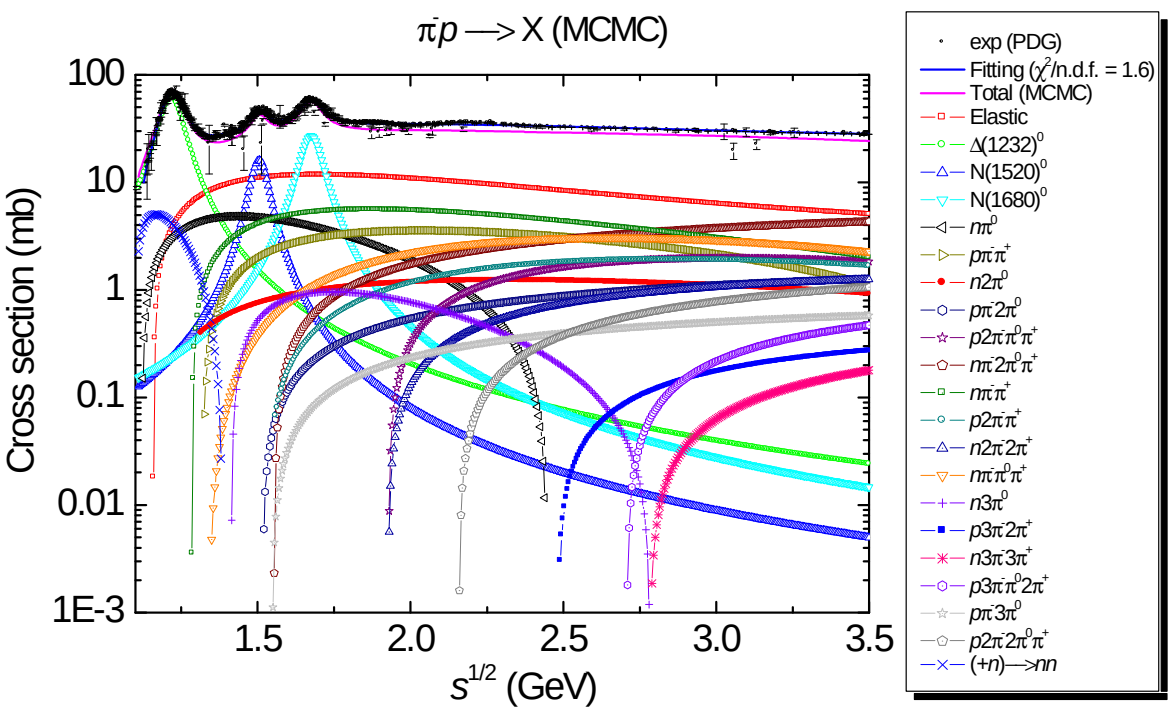

Figure 19: $\pi^- p \longrightarrow X$ channels implemented in the MCMC model. The data points were taken from the PDG.

3.5.1 The elastic $\pi^0 N \to \pi^0 N$ channel

The elastic $\pi^0 N \to \pi^0 N$ channel consists of the most important contribution ($\sim 20\%$) of the total $\pi^0 N$ cross section within the PrimEx kinematics and is also an important source of high energy neutral pions at forward angles. Many other channels can also contribute in the quasi-elastic domain. For instance, a charged pion photoproduction can contribute to the π^0 yield via a charge-exchange process. Fortunately, the probability for a two-body charge exchange goes to zero above $\sqrt{s} \approx 2.5$ GeV (see figs. 17 and 18) and these processes can be safely neglected within the PrimEx kinematics ($E_{\pi^0} \approx k$). On the other hand, the decay of the vector mesons ρ and ω into the π^0 channel can contribute significantly in the hadronic background of neutral pions. Specifically, the channel $\omega \to \pi^0\gamma$ is expected to play an important role at forward angles due to the combination of three factors: i) a huge diffractive ω photoproduction in nuclei, ii) a significant branching ratio for the $\omega \to \pi^0\gamma$ decay (8.5%) and, iii) a favorable kinematics for the production of high energy and forward peaked pions in the $\omega \to \pi^0\gamma$ decay. The contribution of the $\omega \to \pi^0\gamma$ decay in the PrimEx data was estimated using the MCMC model and also in ref.[31], but is not addressed in the present note, which is specifically devoted for the NI π^0 photoproduction.

The differential cross section for elastic πN scattering in the center of mass frame is assumed to be in the form[32]:

$$\left(\frac{d\sigma}{d\Omega}\right)_{\pi N \to \pi N} = \frac{\sigma_T(p)}{\sigma_T(p_0)} \exp\left(a + bt + ct^2\right), \tag{36}$$

where $p_0 = 20$ GeV/c. The total πN cross section can be approximated using the parameterization:

$$\sigma_T(p) = 23.01 + \frac{20.48}{p(GeV/c)}, \text{ for } \pi^+ \text{ and} \tag{37}$$

$$\sigma_T(p) = 24.1 + \frac{26.78}{p(GeV/c)}, \text{ for } \pi^-. \tag{38}$$

The parameters a, b and c are the best fit parameters to the available data within 6 to 20 GeV and are given by:

$$\begin{aligned}
a &= 3.60 \pm 0.05 \\
b &= 8.8 \pm 0.3 \text{ (GeV/c)}^{-2} \\
c &= 2.3 \pm 0.4 \text{ (GeV/c)}^{-4}, \text{ for } \pi^+ \text{ and} \\
a &= 3.65 \pm 0.05 \\
b &= 9.5 \pm 0.3 \text{ (GeV/c)}^{-2} \\
c &= 2.7 \pm 0.4 \text{ (GeV/c)}^{-4}, \text{ for } \pi^-.
\end{aligned}$$

The differential cross sections for the elastic $\pi^{+(-)}p \rightarrow \pi^{+(-)}p$ scattering within the PrimEx kinematics are presented in figures 20 to 24 together with the available data. Figure 20 shows the prediction of eq. (36) for $p = 4.95$ GeV/c in comparison with the data of ref.[33]. Figures 21 and 22 present the results obtained at $p = 7.0$ GeV/c and $p = 6.8$ GeV/c for π^- and π^+, respectively, in comparison with the data of ref.[34]. Figures 23 and 24 show the proposed parameterization at $p = 7.76$ GeV/c and $p = 7.89$ GeV/c for π^+ and π^-, respectively, together with the data from ref.[35]. It is worth-mentioning, however, that the later data include a sizable Coulomb contribution at forward angles. Such contribution is obviously absent in eq.(36), which includes only the strong part and is intended to reproduce the data only at larger angles.

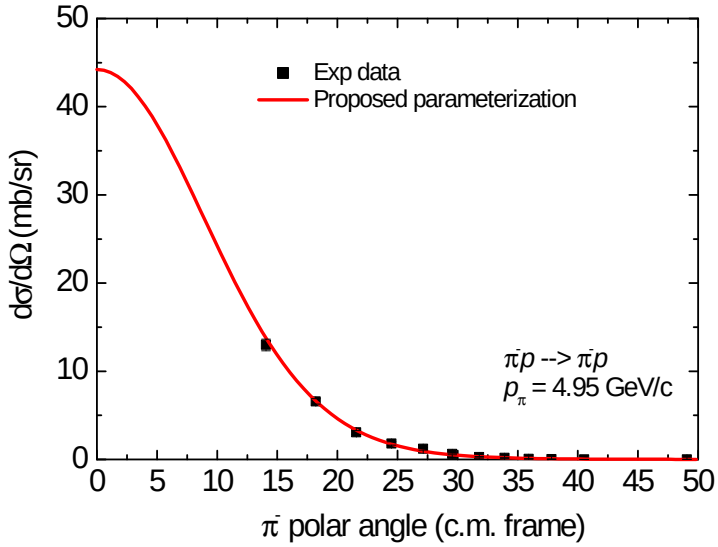

Figure 20: $\pi^- p \longrightarrow \pi^- p$ differential cross section at $p = 4.95$ GeV/c. The data points were taken from ref.[33].

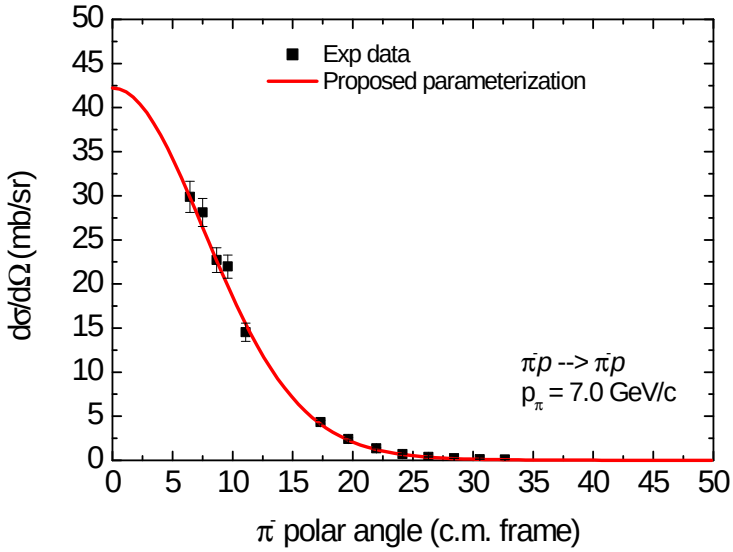

Figure 21: $\pi^- p \longrightarrow \pi^- p$ differential cross section at $p = 7.0$ GeV/c. The data points were taken from ref.[34].

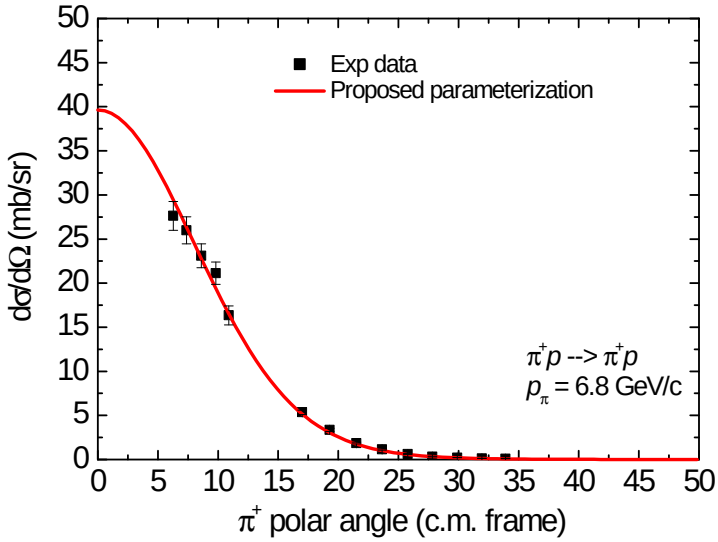

Figure 22: $\pi^+p \longrightarrow \pi^+p$ differential cross section at $p = 6.8$ GeV/c. The data points were taken from ref.[34].

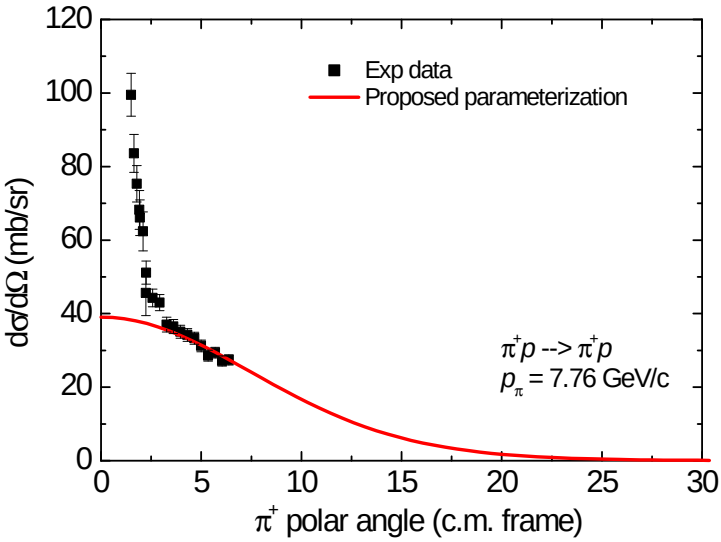

Figure 23: $\pi^+p \longrightarrow \pi^+p$ differential cross section at $p = 7.76$ GeV/c. The data points were taken from ref.[35].

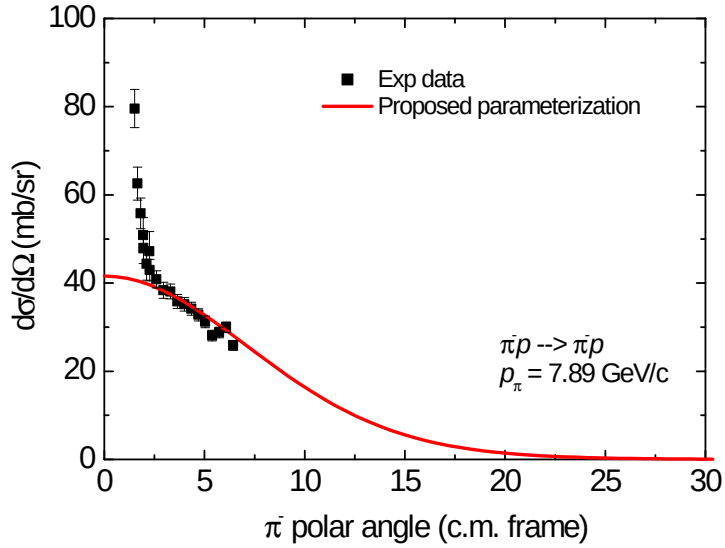

Figure 24: $\pi^- p \rightarrow \pi^- p$ differential cross section at $p = 7.89$ GeV/c. The data points were taken from ref.[35].

The differential cross section for the elastic $\pi^0 N \rightarrow \pi^0 N$ scattering can be deduced from the results obtained for charged pions using the symmetries of the strong interaction and neglecting the Coulomb part:

$$\left(\frac{d\sigma}{d\Omega}\right)_{\pi^0 N \rightarrow \pi^0 N} \cong \frac{1}{2}\left[\left(\frac{d\sigma}{d\Omega}\right)_{\pi^+ p \rightarrow \pi^+ p} + \left(\frac{d\sigma}{d\Omega}\right)_{\pi^- p \rightarrow \pi^- p}\right]. \tag{39}$$

The result of the differential cross section at the mean energy of 5.2 GeV is presented in figure 25.

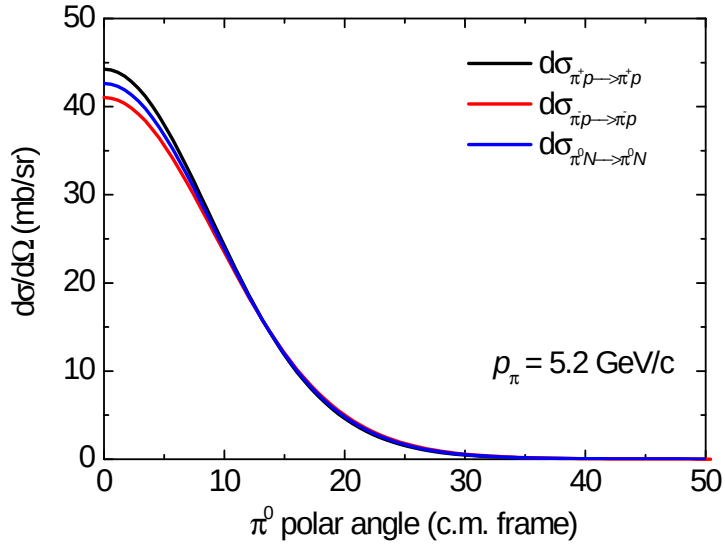

Figure 25: $\pi N \longrightarrow \pi N$ differential cross section at $p = 5.2$ GeV/c. The black and red lines are obtained with eq.(36) for π^+ and π^-, respectively, while the blue line represents the MCMC input for $\pi^0 N \longrightarrow \pi^0 N$.

3.5.2 Pauli-blocking in secondary $\pi^0 N$ scatterings

One of the main hypotheses of the multiple-scattering formalism developed by Glauber is that the nuclear correlations are not relevant during secondary πN scatterings. In this model, the amplitude for πN scattering in the nucleus is approximated by the same quantity for the vacuum, which is the same of neglecting the phase space reduction due to the Pauli principle. In the MCMC model, however, the non-stochastic Pauli-blocking approach propitiates a time-dependent analysis of multiple $p-h$ excitations during the cascade process. The method is completely new and provides a more rigorous formalism to address short range correlations in nuclear matter in comparison with the statistical approaches employed in similar cascade models, such as the Liège INC model [36], as well as in other refined transport calculations[37].

In order to evaluate the influence of the Pauli-principle during secondary scatterings, we have run

the cascade model with and without the Pauli-blocking, collecting any given binary $\pi^0 N$ collision as a function of the intranuclear cascade time. The final results are extremely sensitive to the kinematical cuts in the pion elasticity $\left(\varepsilon_{\pi 0} = \frac{E_{\pi^0}}{k}\right)$([9]). The higher is the pion elasticity ($E_{\pi^0} \approx k$), the lower is the $\pi^0 N$ scattering angle and the higher is the fraction of Pauli-blocked events. On the other hand, for extremely inelastic events ($\varepsilon_{\pi 0} \ll 1$), the pion´s ability to interact is strongly reduced and the fraction of blocked events increases. So, the realistic picture can be achieved using elasticity cuts compatible with the PrimEx analyses and the MCMC accuracy. The results of the time derivative of the average number of $\pi^0 N$ scatterings during a typical cascade at $k = 5.2$ GeV are presented in figures 26 and 27 for Carbon and Lead, respectively. The total number of scatterings is obtained by the integral $\int \frac{d\mathrm{N}}{d\mathrm{t}} d\mathrm{t}$ and the ratio between Pauli-allowed and the total number of scatterings $\left(r^{\mathrm{Pauli}} = \frac{N^{\mathrm{Pauli}}}{N^{\mathrm{Total}}}\right)$ gives the fraction of unblocked events. The fraction of unblocked events is 0.995 (0.956) for Carbon and 0.983 (0.938) for Lead taking into account an isotropic (diffractive) $\pi^0 N$ elastic scattering. The results show consistently that the Pauli-principle affects 5 to 6 % of all the binary events (considering the realistic diffractive distribution) during the cascade stage and should be included for the calculation of the NI cross section. Considering that the Pauli-principle affects more significantly the elastic channel, we can estimate that approximately 25 % of the elastic $\pi^0 N$ scatterings are being blocked, since this mechanism accounts for approximately 20 % of the total $\pi^0 N$ cross section.

[9] The pion elasticity constraint is imposed during the cascade process, which is interrupted after the pion energy has dropped below a cutoff value. For the case of Carbon, the cascade model was run in the range from $\varepsilon = 0.82$ to $\varepsilon = 1.00$ in steps of 0.02, while for Lead only a single run with $\varepsilon = 0.92$ was performed. These values are compatible with the PrimEx analyses in progress and can be further adjusted to cover any specific kinematical cut. However, as we have mentioned before, the accuracy of the model decreases substantially for extremely inelastic events.

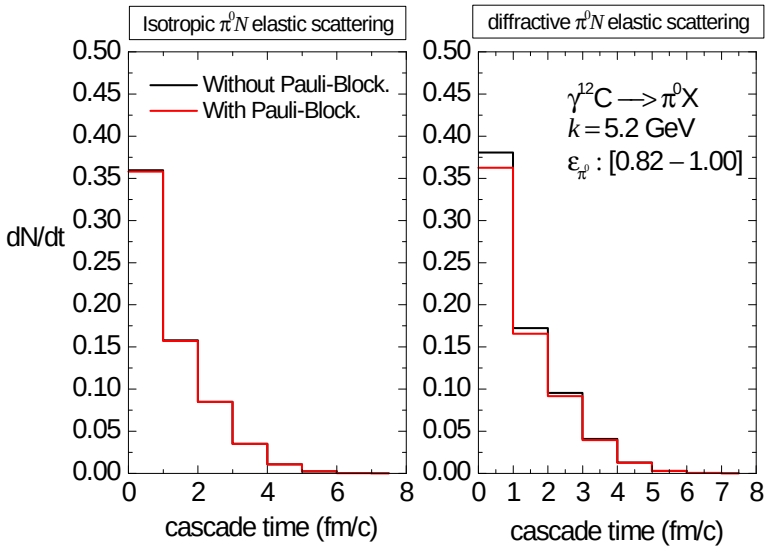

Figure 26: Time derivative of the average number of secondary $\pi^0 N$ scatterings on ^{12}C at $k = 5.2$ GeV as a function of the cascade time. The left panel is obtained assuming an isotropic $\pi^0 N$ elastic scattering, while the right panel shows the results using the parameterization of eq. (39). The black/red histograms were obtained without/with the Pauli-principle taking into account elasticity cut of 0.82.

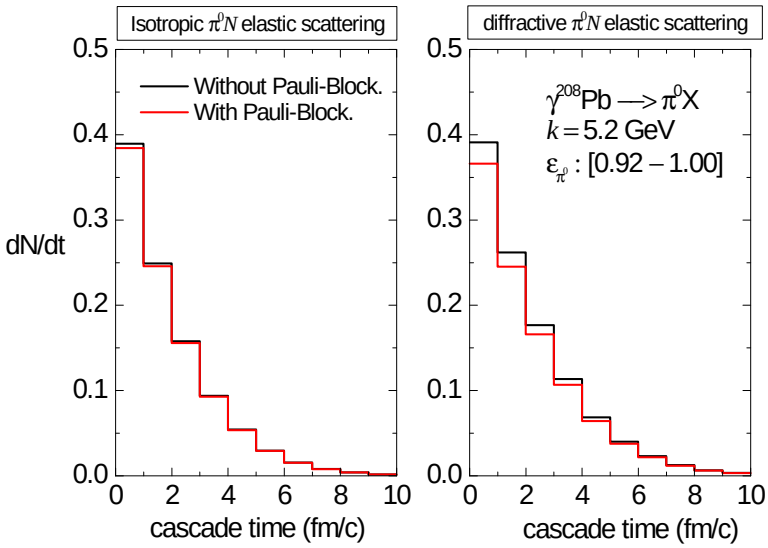

Figure 27: Time derivative of the average number of secondary $\pi^0 N$ scatterings on ^{208}Pb at $k = 5.2$ GeV as a function of the cascade time. The notation is the same of Fig. 26.

4 RESULTS

4.1 Single differential cross sections for incoherent π^0 photoproduction from Carbon and Lead

The single differential cross section for incoherent π^0 photoproduction from complex nuclei is calculated using the elementary photoproduction cross section presented in section 2 and the steps delineated in the previous section. The former introduces the dynamics of the photoproduction mechanism and also the normalization of the final results, such as:

$$\left(\frac{d\sigma}{d\Omega}\right)_A^{PWIA} = A\left(\frac{d\sigma}{d\Omega}\right)_N . \tag{40}$$

The other steps introduce the effects of the nuclear matter, such as the Pauli-blocking during the photoproduction, and the $\pi^0 - nucleus$ FSI. The final result of the NI cross section is then obtained after running the cascade model:

$$\left(\frac{d\sigma}{d\Omega}\right)_A^{PWIA} : \text{— Pauli —>} \left(\frac{d\sigma}{d\Omega}\right)_A^{PB} : \text{— MCMC —>} \left(\frac{d\sigma}{d\Omega}\right)_A^{FSI} . \tag{41}$$

The nuclear shadowing does not change the shape of the cross sections, and:

$$\left(\frac{d\sigma}{d\Omega}\right)_A^{FSI+SHAD} = \frac{A_{eff}^{abs}}{A}\left(\frac{d\sigma}{d\Omega}\right)_A^{FSI} , \tag{42}$$

with $\frac{A_{eff}^{abs}}{A} = 0.76$ for Carbon and 0.75 for Lead. The results for Carbon at 5.2 GeV taking into account an elasticity cut on the pion energy of 0.92 are presented in figure 28.

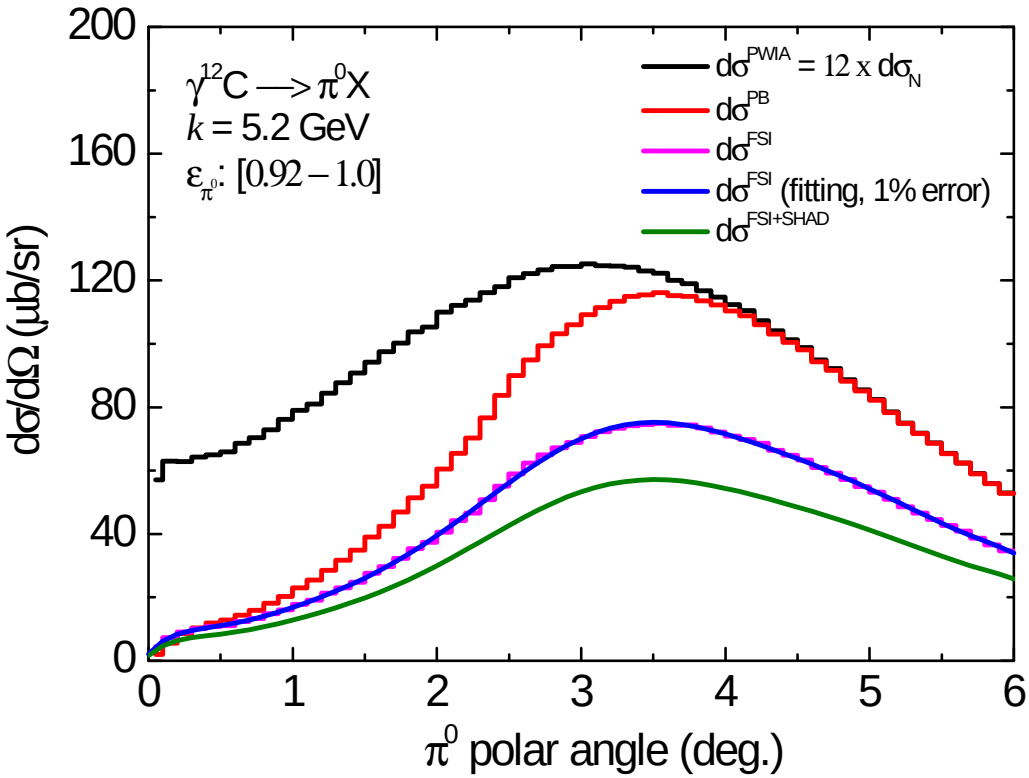

Figure 28: Nuclear Incoherent (NI) cross section for π^0 photoproduction from Carbon. The black histogram is the PWIA, which is A times the single nucleon cross section. The red histogram includes the Pauli-principle during the photoproduction, while the magenta represents the full calculation after including the $\pi^0 - nucleus$ FSI. The blue/olive line is a polynomial fitting that reproduces the results without/with shadowing within 1 % error.

The result for Lead is presented in figure 29. The full FSI results without shadowing for Carbon and Lead (magenta histograms) were fitted using polynomial functions for future and more convenient applications:

$$\left(\frac{d\sigma}{d\Omega}\right)_A^{FSI} = \sum_{i=0}^{i=i_{\max}} a_i \left(\theta_\pi\right)^i , \tag{43}$$

where $\theta_\pi(\deg.)$ is the polar angle of the pion in the laboratory frame. Table 3 summarizes the fitting results that reproduce the histograms within 1%.

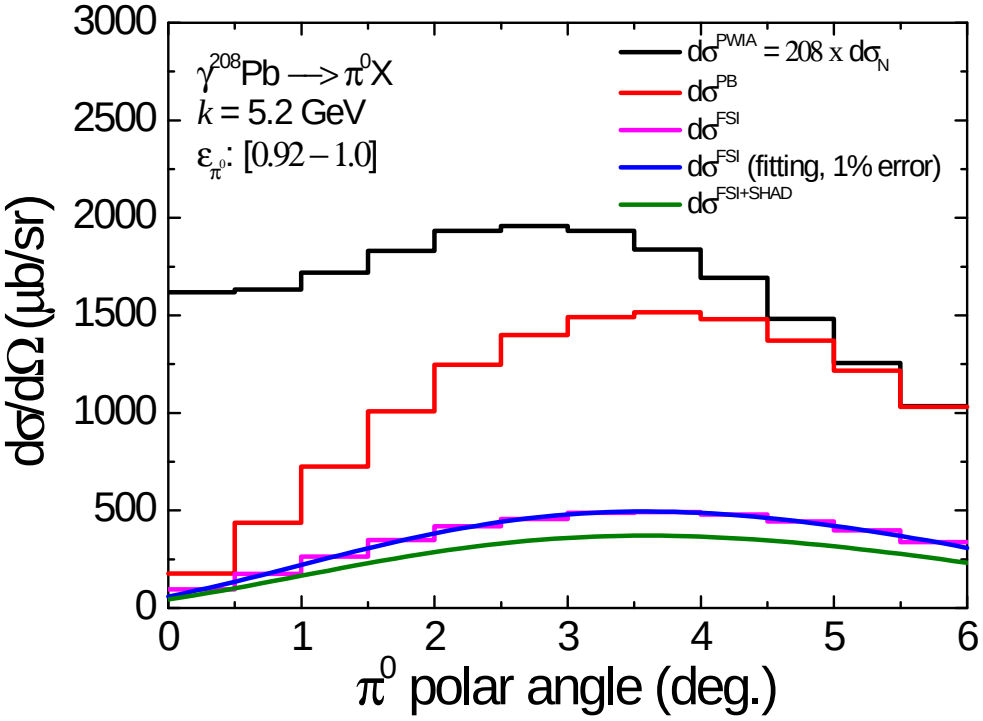

Figure 29: Nuclear Incoherent (NI) cross section for π^0 photoproduction from Lead. The black histogram is the PWIA, which is A times the single nucleon cross section. The red histogram includes the Pauli-principle during the photoproduction, while the magenta represents the full calculation after including the $\pi^0 - nucleus$ FSI. The blue/olive line is a polynomial fitting that reproduces the results without/with shadowing within 1 % error.

	Carbon	Lead
a_0	2.13693196	59.24701
a_1	54.32100061	134.02732
a_2	-162.03473416	41.78831
a_3	280.12168380	-13.7039
a_4	-269.78675670	-0.97941
a_5	158.57390830	0.47206
a_6	-57.96824975	-0.03217
a_7	13.15222467	0
a_8	-1.79891207	0
a_9	0.13584753	0
a_{10}	-0.00435214	0
χ^2_{red}	1.24	1.27

Table 3: Fitting parameters of the NI cross sections without shadowing. Details in the text.

4.2 Double differential cross sections for incoherent π^0 photoproduction from Carbon and Lead

The double differential cross section for incoherent π^0 photoproduction from complex nuclei is the most convenient observable for the evaluation of the hadronic background at forward angles. Such theoretical prediction propitiates the construction of realistic event generators of the NI mechanism, since it includes the information about the energy losses due to the nuclear excitation either with or without secondary meson-nucleus interactions. Different kinematical cuts may take place in different analyses and the double differential cross section could provide a consistent explanation for possible variations in the absolute cross sections at larger angles. At extreme forward angles, the pion energies are very close to the photon energy and different kinematical cuts should lead to similar and consistent results. At larger angles, on the other hand, the shape of the NI cross section is very sensitive to the cuts made on the pion energy and small differences in the choice of the elasticity cut could lead to different results in shape and magnitude. The double differential cross section as a function of the pion polar angle $\frac{d^2\sigma}{d\theta dE_{\pi^0}}$ is calculated in the Monte Carlo algorithm taking into account the same kinematical cuts applied for the single differential cross section, satisfying the normalization:

$$\int \left(\frac{d^2\sigma}{d\theta dE_{\pi^0}}\right)_A^{FSI} dE_{\pi^0} = 2\pi \sin\theta \left(\frac{d\sigma}{d\Omega}\right)_A^{FSI} .$$

The results obtained for Carbon at $\varepsilon_{\pi^0} \geq 0.92$ are presented at selected polar angles in Fig. 30. The pion spectra exhibit a sharp peak close to the photon energy at lower angles, since the nuclear excitation is quite small for low momentum transfer. The effect of the Pauli-principle is also observed for lower angles, where the pion spectrum decreases about one order of magnitude

from 1.25 to 0.25 degrees.

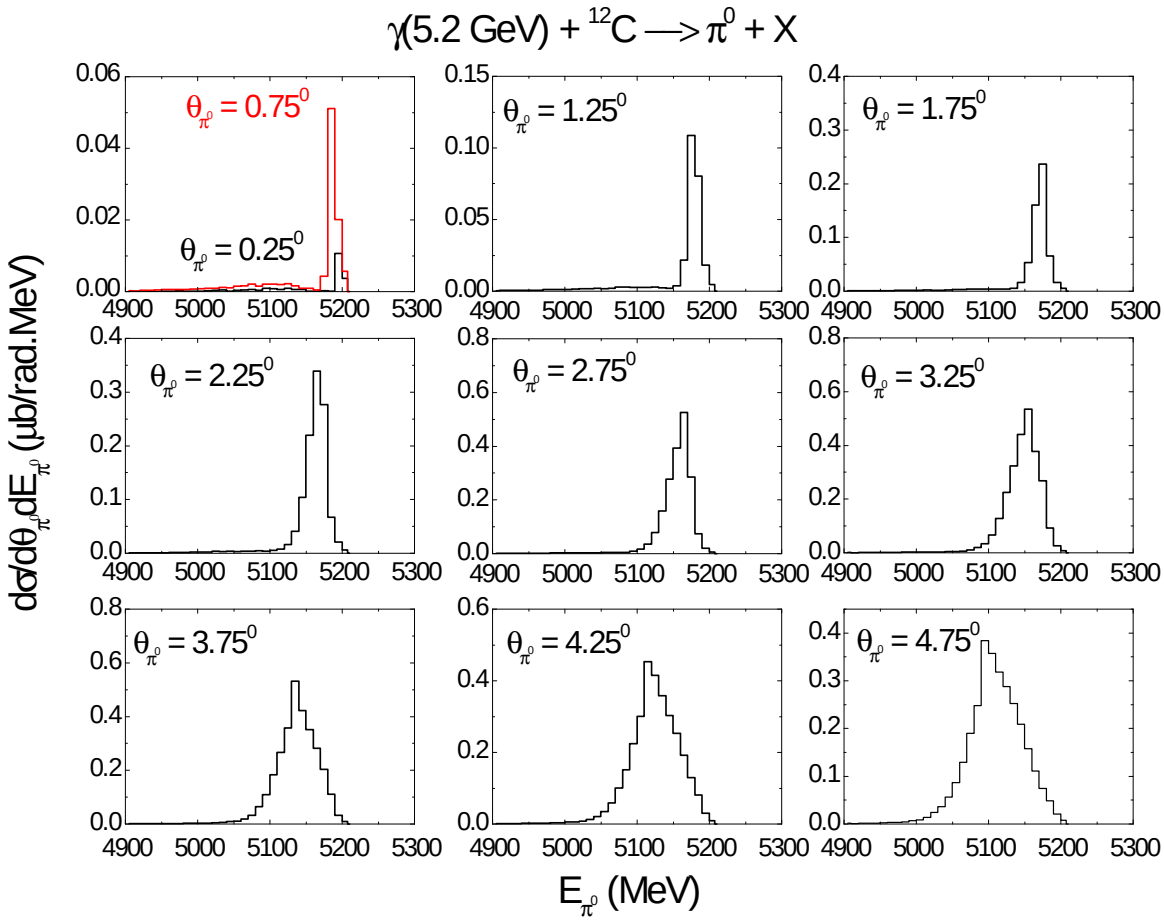

Figure 30: Double differential cross section for incoherent π^0 photoproduction from Carbon. The histograms represent the full calculation without shadowing.

The results for Lead are presented in Fig. 31, where one easily observes similar peaks near the photon energy at low polar angles. For higher angles, however, broad energy distributions are obtained due to a much larger phase space. The pion spectra both for Carbon and Lead are always concentrated within approximately k and $k - 200$ MeV at polar angles up to 4.75 degrees.

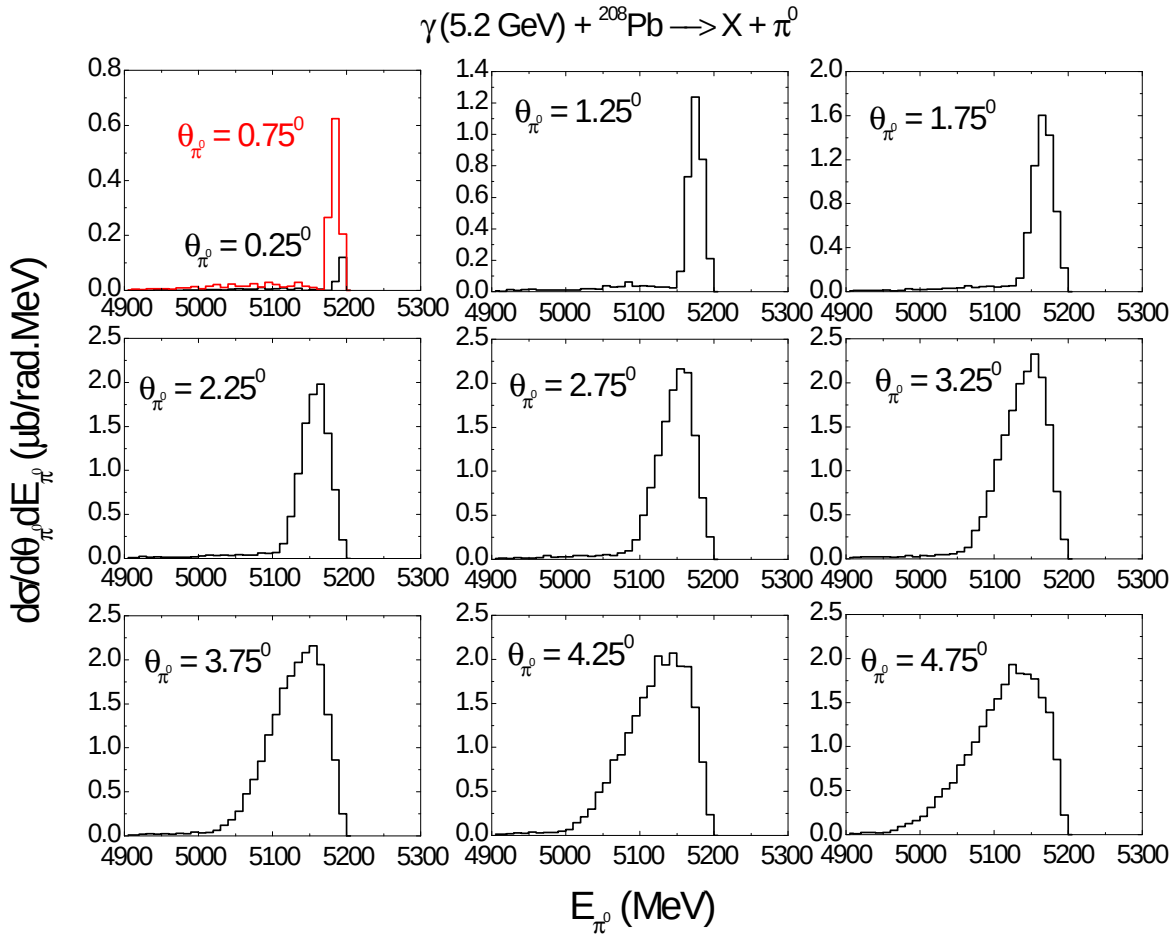

Figure 31: Double differential cross section for incoherent π^0 photoproduction from Lead. The histograms represent the full calculation without shadowing.

4.3 π^0 energy spectra due to incoherent production from Carbon and Lead

The pion spectrum due to incoherent production is another observable useful to delineate the hadronic background. The pion spectra due to coherent production (Primakoff/Nuclear Coherent) are known to be concentrated within typically k and $k - 10$ MeV[7], region where the incoherent part does not vanish but is quite small. On the other hand, below $k - 10$ MeV, only the inelastic part survives and the total pion spectra could be approximated by the sum of the NI part and the decay of heavier mesons, such as ρ and ω. So, to the extent that the adopted inelastic domain ($\varepsilon_{\pi^0} \geq 0.92$) satisfies the PrimEx environment, one can calculate the pion spectra directly from the Monte Carlo. The spectra are normalized such that:

$$\int \left(\frac{d\sigma}{dE_{\pi^0}}\right)_A^{FSI} dE_{\pi^0} = \int \left(\frac{d\sigma}{d\Omega}\right)_A^{FSI} d\Omega.$$

The results for Carbon and Lead (without shadowing) are presented in figure 32. Both spectra present a smooth decrease from $E_{\pi^0} \approx k - 30$ MeV to $E_{\pi^0} \approx k$ due to the Pauli-principle, since this region corresponds to pion production at extreme forward angles. It is also observed that the pion spectra due to incoherent production do not vanish within the quasi-elastic domain of coherent production ($E_{\pi^0} \gtrsim k - 10$ MeV), showing that the inelastic part can not be disentangled from the coherent part using only the information of the pion energy distribution. Also, the energy resolution of the PrimEx experiment (two photon cluster energy resolution) is not likely to allow an accurate determination of the details of the pion spectra in such a narrow energy range. The distributions present a clear flat shape for pions with lower energies (higher momentum transfer) since the Pauli-principle is less relevant in this region.

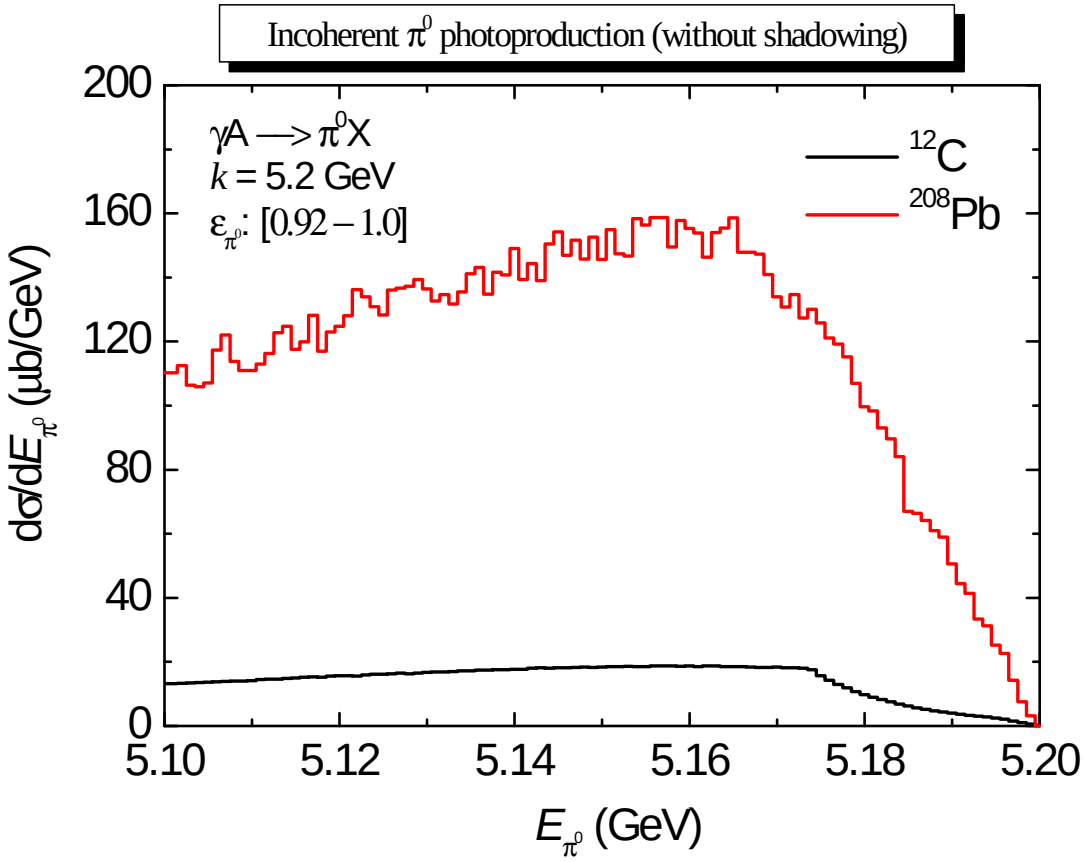

Figure 32: π^0 energy spectra due to incoherent production from Carbon (black) and Lead (red) including full FSI of the produced pions. The results are for pion elasticity grater than 0.92 and do not include shadowing.

4.4 Revisiting the NI cross section for Carbon

4.4.1 NI cross section versus MD parameterization

As previously mentioned in this note, we have also run the cascade model for Carbon taking into account different sets of momentum distributions in order to evaluate the sensitivity of the model with respect to this important input. The runs were made combining $1s$ and $1p$ proton knock-out data obtained at different facilities as sketched in table 4.

$s-$shell	$p-$shell	cascade run #
PWIA[21]	PWIA[21]	1 (main run)
Saclay 76[22]	Saclay 76[22]	2
Saclay 76[22]	Saclay 82[23] (perp.)	3
Saclay76[22]	Saclay 82[23] (par.)	4
Tokyo 76[24]	Tokyo 76[24]	5
Nikhef 88[25]	Nikheff 88[25]	6

Table 4: Different sets of momentum distributions for the s and p shells of Carbon used in the present analysis.

The results of the differential cross sections $\left(\frac{d\sigma}{d\theta} = 2\pi \sin\theta \frac{d\sigma}{d\Omega}\right)$ including full FSI are presented in figure 33 for the six runs considered. The absolute differences between the NI cross sections of runs 2 to 6 and main run 1 are shown in figure 34, where one easily verifies that the cascade results are safely concentrated within 2 $\mu b/rad$ from 0 to 4 degrees. The differences do not exceed 0.5 $\mu b/rad$ up to approximately 0.5 degrees.

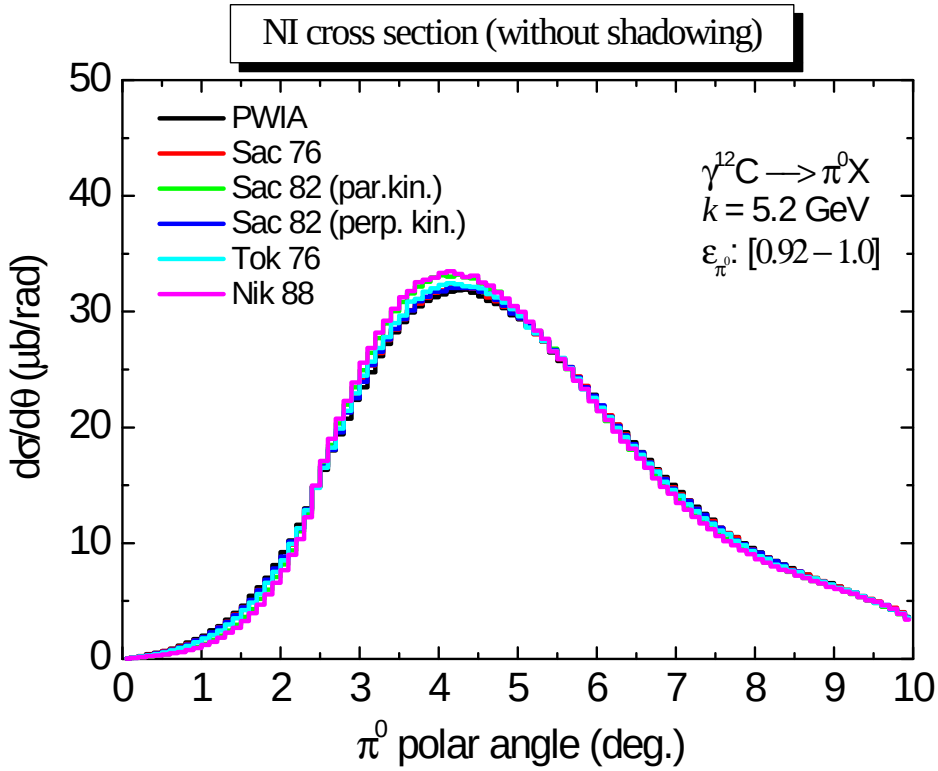

Figure 33: Differential cross section $\left(\frac{d\sigma}{d\theta}\right)$ of incoherent π^0 photoproduction from Carbon as a function of the MD parameterization.

In order to verify the consistency of the results, we have averaged the NI cross section between runs 2 to 6 and compared this result, with one standard deviation, with the one obtained in main run 1. Figure 35 shows the averaged NI cross section from runs 2 to 6 in comparison with run 1. A nice agreement between the results is verified, making it possible to estimate a systematic uncertainty in our main run # 1 due to the MD parameterization. This uncertainty can be estimated by the relative difference (RD) between main run 1 and the average from runs 2 to 6, which is presented in figure 36.

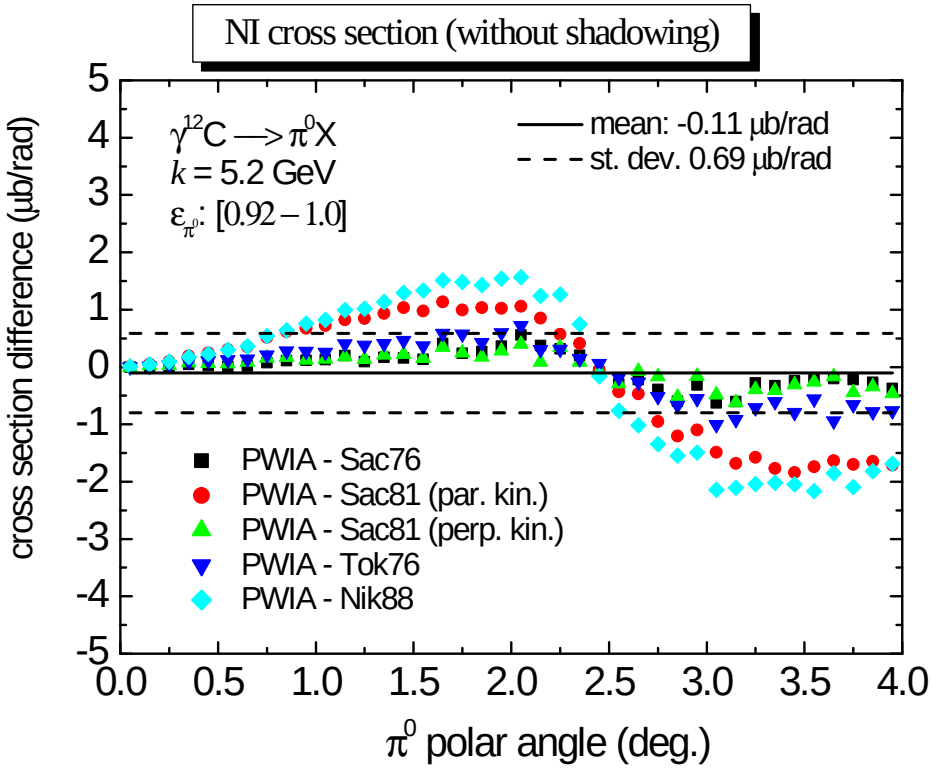

Figure 34: Absolute differences between the NI cross section obtained from main run 1 and run 2 to 6. The average of the differences is $-0.11 \pm 0.69\ \mu b/rad$ from 0 to 4 degrees.

The relative difference (%) so obtained was fitted assuming a polynomial function:

$$\mathrm{RD}(Q^2) = \sum_{i=0}^{6} b_i \left(Q^2\right)^i, \tag{44}$$

where $Q^2(GeV/c)^2$ is the square of the 4-momentum transfer, given by: $Q^2 \cong k^2\theta^2 + \left(\frac{m_\pi^2}{2k}\right)^2$. The fitted parameters b_i are presented in table 5.

b_0	b_1	$b_2(\times 10^3)$	$b_3(\times 10^4)$	$b_4(\times 10^4)$	$b_5(\times 10^4)$	$b_6(\times 10^4)$	χ^2_{red}
25.45	-710.25	5.984	-2.282	4.43	-4.27	1.61	0.88

Table 5: Fitting parameters of the relative difference presented in figure 36.

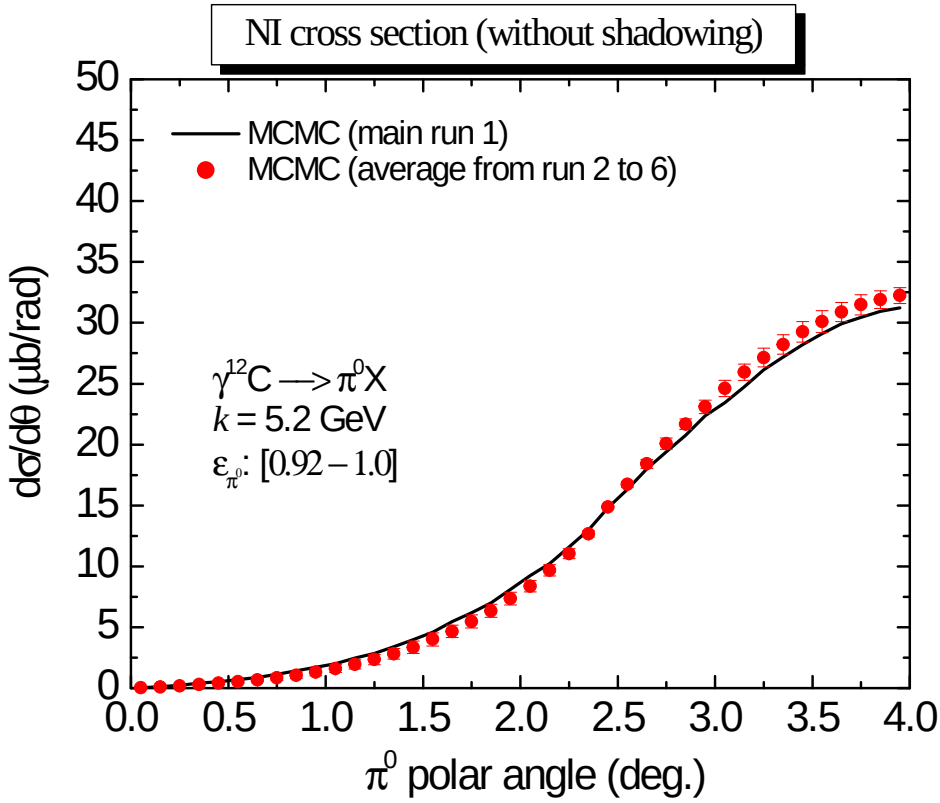

Figure 35: NI cross section from main run 1 (black line) and the average value from run 2 to 6 with one standard deviation (red points).

Figure 37 presents the RD as a function of Q^2 for future reference. With this approach, the sensitivity of the cascade model due to the MD parameterization for Carbon is estimated and can be propagated to the final results (with or without shadowing) in order to provide a range of confidence in the model predictions.

Finally, figure 38 shows the predictions of the cascade model for the NI cross section taking into account the relative difference obtained with different MD parameterizations. The upper and lower histograms represent the results for run 1 plus and minus the fitted relative difference, respectively. It is worth mentioning, however, that the same procedure can be applied to the double differential cross section and also to the results that include shadowing, since the later does not change the

shape of the cross sections.

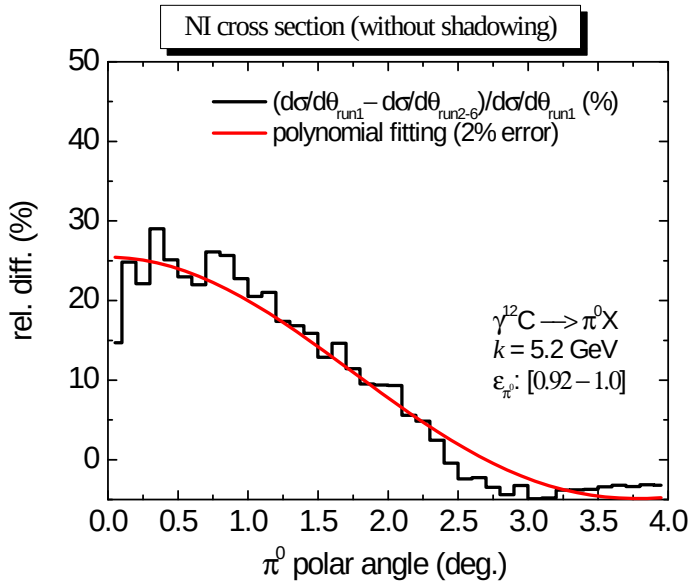

Figure 36: Relative difference (%) between main run 1 and the average from runs 2 to 6. The polynomial fitting reproduces the relative difference within $\pm 2\%$.

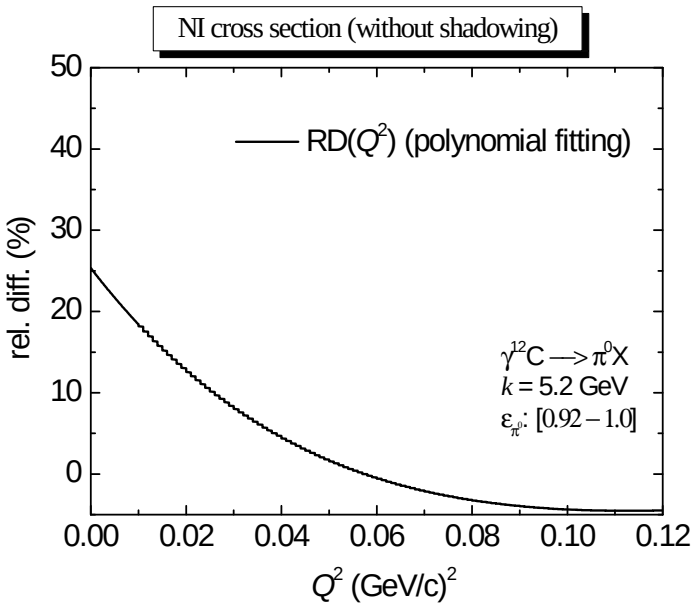

Figure 37: Relative difference (%) as a function of Q^2. Details in the text.

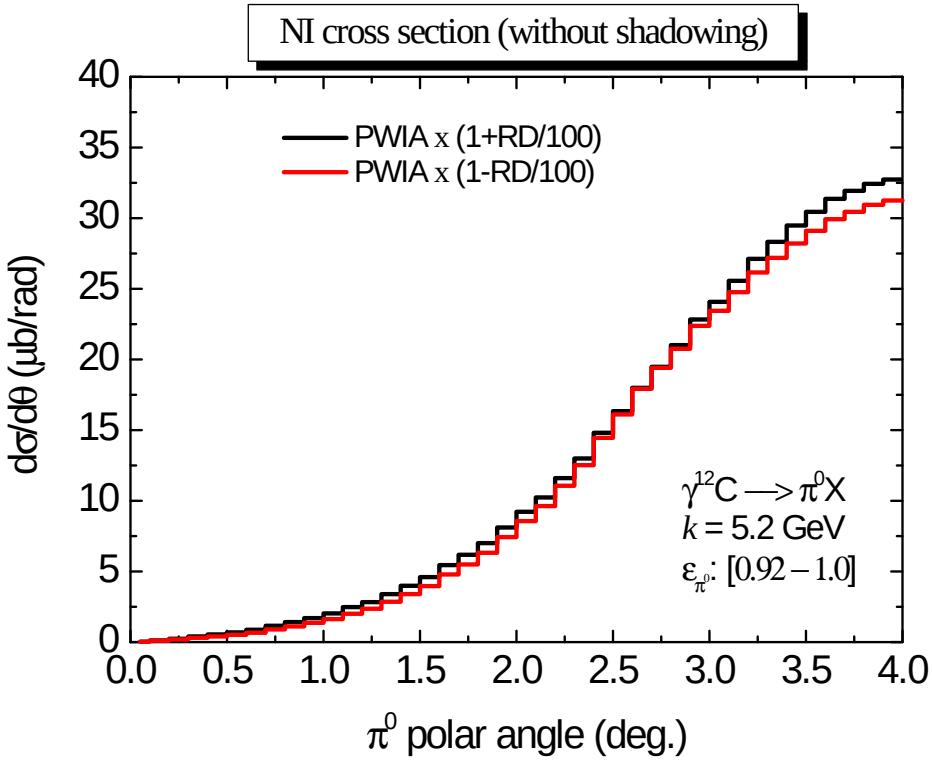

Figure 38: Upper and lower limits of the Nuclear Incoherent cross section for π^0 photoproduction from Carbon obtained via the MCMC model.

4.4.2 NI cross section versus π^0 elasticity

In this section, we investigate the influence of cuts in π^0 elasticity on the shape and magnitude of the NI cross section at small angles. The NI cross section at forward angles is expected to depend very critically on kinematical cuts, since the momentum transfers are very small and the total energy carried out by the pion is sensitive to the nuclear excitation, as well as to the secondary elastic scatterings at small angles. These secondary scatterings are more likely to contribute at forward angles due to the diffractive behavior of the elementary $\pi^0 N \rightarrow \pi^0 N$ process. So, any calculation that provides information about the pion energy losses during multiple scatterings should include such constraint to the elastic channel. Figure 39 shows the NI cross section $\left(\frac{d\sigma}{d\Omega}\right)$ for π^0 photopro-

duction at selected pion elasticity. The contribution of secondary scatterings at forward angles is evident if we consider the increasing difference between the NI cross section for wider elasticity cuts. This result indicates that relaxing the elasticity cut has the natural effect of increasing the background also at forward angles due to secondary scatterings. The result for $\varepsilon_{\pi^0} : [0.98 - 1.00]$ (olive line) decreases very fast above approximately 3 degrees as a consequence of the higher momentum transfer carried out by the struck nucleon.

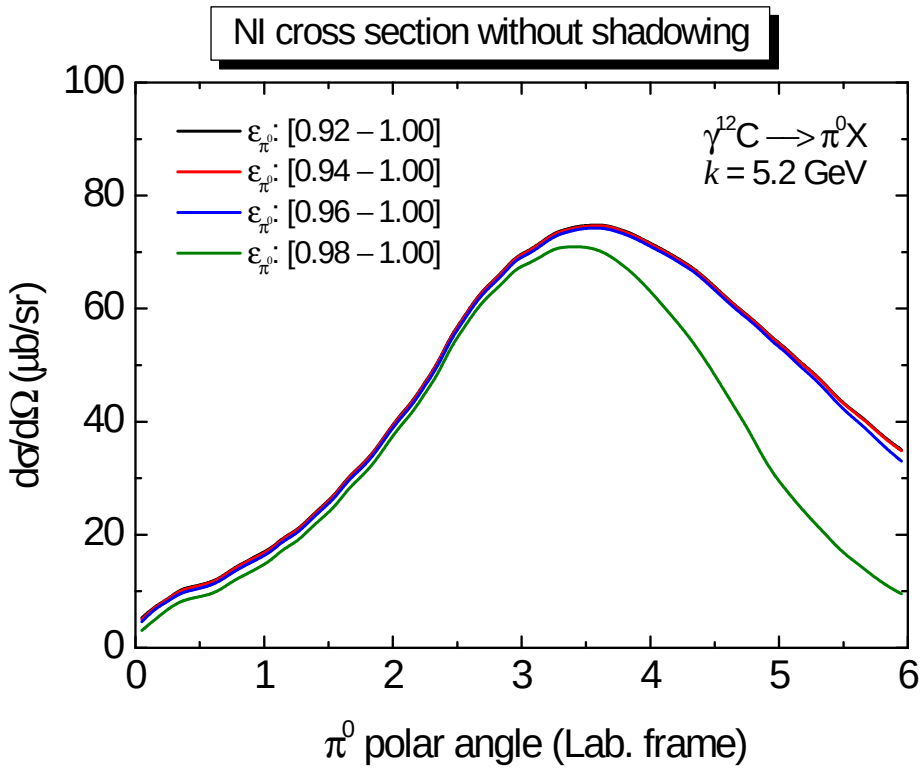

Figure 39: Nuclear Incoherent cross section for π^0 photoproduction from Carbon as a function of pion elasticity.

Figure 40 presents the absolute cross section differences between two distinct kinematical cuts. It is also evident from figure 40 that relaxing the cuts on pion energy increases the π^0 background isotropically up to 4 degrees. This fact reinforces the idea of using the double differential cross section to delineate the π^0 background and make theory and experiment mutually consistent.

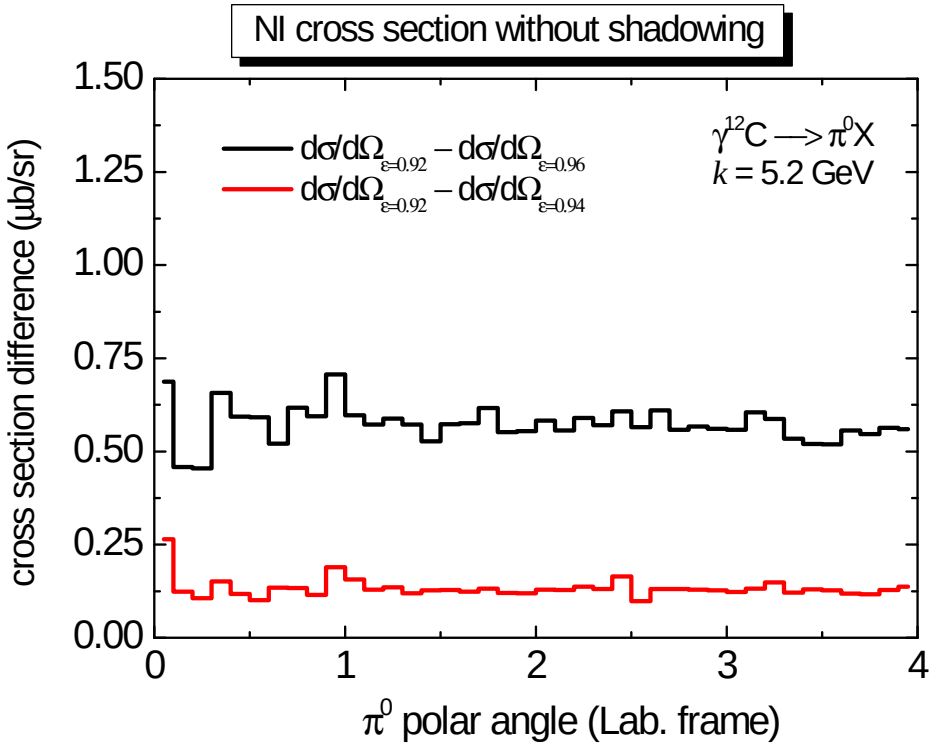

Figure 40: Absolute cross section differences between the NI cross section at distinct kinematical cuts.

4.5 A_{eff} factor for incoherent π^0 photoproduction from Carbon and Lead: Comparing the MCMC predictions with the available data.

The A_{eff} factor for incoherent π^0 photoproduction from the nucleus is one of the most important step towards the determination of the magnitude of the NI cross section. Although the $\pi^0 \to \gamma\gamma$ decay width is only sensitive to the shape - instead of the magnitude - of the NI cross section; it is also extremely relevant to verify that the nuclear background in the PrimEx data could be interpreted in shape and magnitude as a non-diffractive incoherent mechanism. Such condition would provide a clear verification that the inelastic background is completely under control for future experiments. The A_{eff} factor for π^0 photoproduction is assumed to be the ratio between the measured cross section from the nucleus and that from the nucleon:

$$A_{eff}^{\pi^0} = \frac{\int \left(\frac{d\sigma}{d\Omega}\right)_A d\Omega}{\int \left(\frac{d\sigma}{d\Omega}\right)_N d\Omega}. \tag{45}$$

In PWIA, we have $A_{eff}^{\pi^0} = A$, since $\left(\frac{d\sigma}{d\Omega}\right)_A^{PWIA} = A\left(\frac{d\sigma}{d\Omega}\right)_N$. So, taking into account the Pauli-blocking during the photoproduction, as well as the full FSI of the produced pions, we arrive to the following expression:

$$A_{eff}^{\pi^0}(MCMC) = \frac{\int \left(\frac{d\sigma}{d\Omega}\right)_A^{FSI} d\Omega}{\int \left(\frac{d\sigma}{d\Omega}\right)_N d\Omega}. \tag{46}$$

Alternatively, the $A_{eff}^{\pi^0}$ factor can be calculated using the integral formalism of Glauber. In this model - which does not account for shadowing - the following expression is deduced for high energy pions:

$$A_{eff}^{\pi^0}(Glauber) = \frac{2\pi}{\sigma_{\pi^0 N}} \int_0^\infty \left[1 - \exp\left(-\sigma_{\pi^0 N} \int_{-\infty}^{\infty} N(b,z)dz\right)\right] bdb, \tag{47}$$

where $\sigma_{\pi^0 N}$ is the total $\pi^0 N$ cross section and $N(b,z)$ the nuclear density with $r^2 = b^2 + z^2$. So, eqs. (46) and (47) can provide two different approaches to determine $A^{\pi^0}_{eff}$.

An important measurement of $A^{\pi^0}_{eff}$ for Carbon and Lead was performed in the 70´s at Cornell. In this experiment[19], the π^0 yields from complex nuclei were measured and normalized to the deuteron data, keeping the 4-momentum transfers in the range $0.10 < |t| < 0.25\ (GeV/c)^2$. This procedure did not permit an unambiguous verification of the absolute values of $A^{\pi^0}_{eff}$, since the normalization procedure was model dependent due to the Glauber corrections applied to the π^0 absorption in the deuteron. However, these data represent the only measurements ever made for $A^{\pi^0}_{eff}$, making the confront between theory and experiment an urgent issue. Certainly, future experiments would provide more accurate and model independent $A^{\pi^0}_{eff}$ factors from complex nuclei.

Since the NI cross section largely dominates the π^0 yield from Cornell experiment, we neglect the contribution from the Nuclear Coherent (NC) and Primakoff - Nuclear Coherent interference mechanisms and assume that the total cross section from the nucleus is uniquely attributed to the NI cross section ([10]). So, in order to compare the predictions from the MCMC model with Cornell's data, we have to calculate the differential cross section as a function of t and perform the following integral:

$$A^{\pi^0}_{eff}(MCMC) = \frac{\int_{0.1}^{0.25} \left(\frac{d\sigma}{dt}\right)_A^{FSI} dt}{\int_{0.1}^{0.25} \left(\frac{d\sigma}{dt}\right)_N dt} = A \frac{\int_{0.1}^{0.25} \left(\frac{d\sigma}{dt}\right)_A^{FSI} dt}{\int_{0.1}^{0.25} \left(\frac{d\sigma}{dt}\right)_A^{PWIA} dt}, \tag{48}$$

where we have used the identity $\int_{0.1}^{0.25} \left(\frac{d\sigma}{dt}\right)_A^{PWIA} = A \int_{0.1}^{0.25} \left(\frac{d\sigma}{dt}\right)_N$ in the last step. Figures 41 and 42 present our predictions for the NI cross section from Carbon and Lead as a function of t, in comparison with the PWIA.

[10] The range of momentum transfers from Cornell experiment ($0.10 < |t| < 0.25\ (GeV/c)^2$) guarantees that the NC process does not contribute. However, the contributions from the decay of heavier mesons (ρ and ω) are very relevant within this kinematics, but they were clearly separated in the Cornell experiment[19].

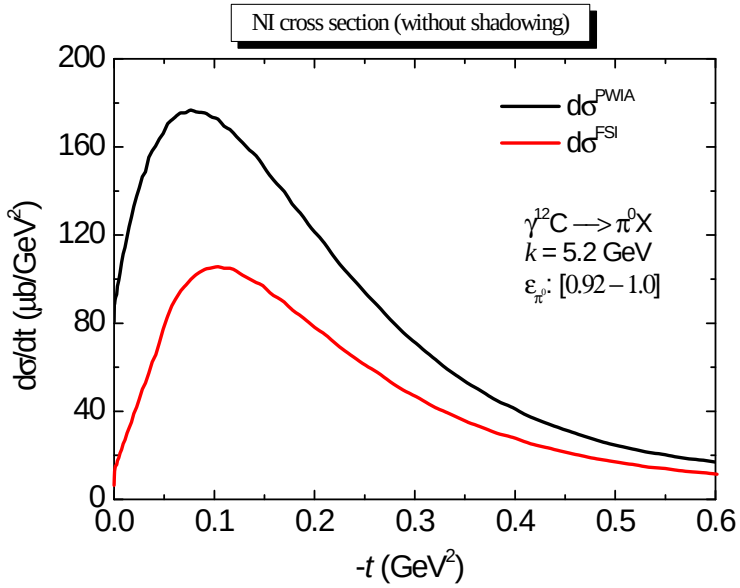

Figure 41: Nuclear Incoherent cross section for π^0 photoproduction from Carbon as a function of t. The black line is the PWIA, while the red line includes the effect of Pauli-blocking and FSI.

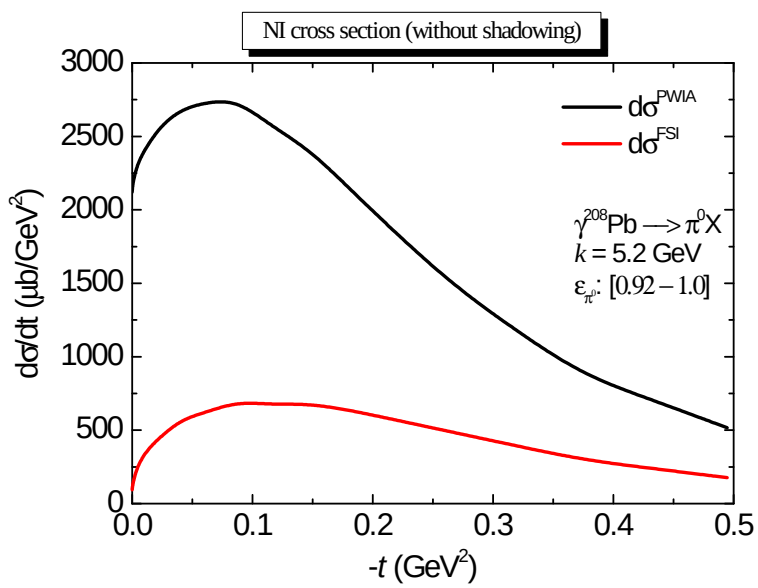

Figure 42: Nuclear Incoherent cross section for π^0 photoproduction from Lead as a function of t. The black line is the PWIA, while the red line includes the effect of Pauli-blocking and FSI.

So, using eqs.(47) and (48), we can calculate the values of $A^{\pi^0}_{eff}$ (without shadowing) both for

Carbon and Lead. The last step is the inclusion of the nuclear shadowing, which is easily done by the multiplication of the MCMC results by 0.76 (Carbon) and 0.75 (Lead). Table 6 presents our results for $A_{eff}^{\pi^0}$ for Carbon and Lead using the MCMC and Glauber models in comparison with the Cornell data.

$A_{eff}^{\pi^0}$	Glauber 5.2 GeV	MCMC 5.2 GeV	MCMC (Shad.) 5.2 GeV	Cornell 4.6 GeV	Cornell 6.4 GeV
Carbon	7.22	7.64	$7.64\times0.76 = 5.82$	5.83 ± 0.30	5.73 ± 0.29
Lead	60.14	60.01	$60.01\times0.75 = 44.65$	41.6 ± 2.4	44.7 ± 2.6

Table 6: A_{eff} factors for π^0 photoproduction from Carbon and Lead obtained using the MCMC and Glauber models in comparison with the Cornell measurements at selected energies.

As clearly observed, both the MCMC and Glauber models give similar results (within $\sim 6\%$) for $A_{eff}^{\pi^0}$ if we neglect shadowing. The inclusion of shadowing decreases $A_{eff}^{\pi^0}$ by approximately 25% and the MCMC results reproduce the Cornell data within the error bars both for Carbon and Lead. The values reported by the Cornell experiment do not present a strong energy dependence and we can safely compare our predictions at $k = 5.2$ GeV, which is the average energy from PrimEx, with the data obtained at Cornell in the range from 4.6 to 6.4 GeV.

5 CONCLUSIONS AND FINAL REMARKS

A sophisticated intranuclear cascade Monte Carlo model was developed for the interpretation of the incoherent π^0 photoproduction from PrimEx experiment. The model, which is based on a relativistic and time dependent multicollisional framework, incorporated important features and improvements with respect to older versions, such as: i) an accurate elementary π^0 photoproduction mechanism based on a Regge model and constrained by the available data to describe the initial photo-nucleus interaction, ii) realistic momentum distributions for Carbon deduced from s and $p-$shells one-nucleon removal experiments, iii) a completely new non-stochastic Pauli-blocking approach for the initial photo-nucleus interaction, as well as in binary $\pi^0 N$ scatterings during the cascade, iv) the analysis of the shadowing effect via the VMD model, and v) the implementation of multiple $\pi^0 N$ processes for the evaluation of the full FSI of the produced pions with the nucleus.

The model presented some special features in comparison with similar transport techniques, since it accounted for the energy losses of the produced pions using relativistic kinematics. Also, the contribution of the elastic $\pi^0 N \rightarrow \pi^0 N$ channel at forward angles was evaluated using realistic (diffractive) angular distributions. The effect of the Pauli-blocking during secondary scatterings - which is generally neglected in other transport models - is considered in our calculations. The diffractive behavior of the process $\pi^0 N \rightarrow \pi^0 N$, which accounts for approximately 20% of the total $\pi^0 N$ cross section, changes the shape of the NI cross section (in comparison with the previous isotropic version) and increases the cross section by about 5 to 15 % both for Carbon and Lead. These effects come from the higher probability of forward scatterings and a stronger Pauli suppression ($\sim$5%)

The calculation of the shadowing effect in high energy photo-nucleus interactions is based on the VMD model and incorporates the *formation time* concept. The nuclear transparencies to vector

mesons are calculated in the MCMC routine and provide qualitative information regarding the attenuation of the physical photon deep in the nuclei. The results for Carbon and Lead are very consistent with previous estimates of other models. It is worth-mentioning, however, that the predictions of the shadowing effect presented in this note represent only crude estimates that are likely to be superseded by the forthcoming PrimEx data. Fortunately, the final result of the $\pi^0 \to \gamma\gamma$ decay width is not sensitive to the normalization of the NI cross section; it depends only on the accurate shape of the hadronic background which is carefully accounted for in this note.

The MCMC model have provided some important observables for future reference, such as: i) the Pauli-blocking factors for π^0 photoproduction from Carbon and Lead, ii) the time derivative of the average number of $\pi^0 N$ scatterings during the *high energy* cascade stage, iii) single differential cross section for incoherent π^0 photoproduction from Carbon and Lead, iv) double differential cross section for incoherent π^0 photoproduction from Carbon and Lead, v) π^0 energy spectra due to incoherent photoproduction, and vi) $A^{\pi^0}_{eff}$ factors both for Carbon and Lead. The single differential cross sections for Carbon and Lead at 5.2 GeV were fitted with polynomial functions for future convenience. The precision of the fitting is 1% for Carbon and 2% for Lead.

The sensitivity of the NI cross section from Carbon due to the momentum distribution (MD) parameterization was evaluated running the cascade model with different sets of parameterizations. The results indicate that the relative difference between the main run 1, which is based on the PWIA for the MD, and the others is more relevant at forward angles due to the Pauli-blocking effect. Fortunately, the absolute differences between these runs were always within 0.5 $\mu b/rad$ up to approximately 0.5 degrees, where the Primakoff cross section is quite small.

A strong dependence of the NI cross section due to the pion elasticity was observed, suggesting that a careful analysis combining the single and double differential cross section would be useful to

bring theory and experiment together.

In conclusion, a detailed calculation based on a Monte Carlo intranuclear cascade algorithm has been proposed for the interpretation of the shape and magnitude of the π^0 incoherent background in the PrimEx experiment. The model provided a consistent method of extracting the $A_{eff}^{\pi^0}$ factors both for Carbon and Lead, reproducing for the first time the Cornell's data within the error bars.

References

[1] http://www.jlab.org/primex/primex_notes/PR99-014.ps (PrimEx proposal).

[2] H. Primakoff, Phys. Rev. **81**, 899 (1951).

[3] G. Faldt, Nucl. Phys. **43**, 591 (1972).

[4] S. Gevorkyan, A. Gasparian, L. Gan and I. Larin, *Incoherent Photoproduction of* π^0 *Mesons off Nuclei*, PrimEx note # 50 (2007).

[5] T. E. Rodrigues, J. D. T. Arruda-Neto, J. Mesa, C. Garcia, K. Shtejer, D. Dale and I. Nakagawa, Phys. Rev. C **71**, 051603(**R**) (2005).

[6] B. Krusche *et al.*, Eur. Phys. J. A **22**, 277 (2004).

[7] T. E. Rodrigues, J. D. T. Arruda-Neto, J. Mesa, C. Garcia, K. Shtejer, D. Dale and I. Nakagawa, Braz. J. of Phys., vol. **36**, no. 4b, 1366 (2006).

[8] T. E. Rodrigues, J. D. T. Arruda-Neto, A. Deppman, V. P. Likhachev, J. Mesa, C. Garcia, K. Shtejer, G. Silva, S. B. Duarte and O. A. P. Tavares, Phys. Rev. C **69**, 064611 (2004).

[9] T. E. Rodrigues, M. N. Martins, C. Garcia, J. D. T. Arruda-Neto, J. Mesa, K. Shtejer and F. Garcia, Phys. Rev. C **75**, 014605 (2007).

[10] T. E. Rodrigues, J. D. T. Arruda-Neto, J. Mesa, C. Garcia, K. Shtejer, D. Dale, I. Nakagawa and P. Cole, Phys. Rev. Lett. **101**, 012301 (2008).

[11] A. Browman *et al.*, Phys. Rev. Lett. **32**, 1067 (1974).

[12] J. S. Ball, Phys. Rev. **124**, 2014 (1961).

[13] G. F. Chew, M. L. Goldberger, F. E. Low and Y. Nambu, Phys. Rev. **106**, 1345 (1957).

[14] A. Gasparian and S. Gevorkyan, "Theoretical part of PrimEx", (private communication, 2004).

[15] J. S. Ball, W. R. Frazer and M. Jacob, Phys. Rev. Lett. **20**, 518 (1968).

[16] M. Braunschweig, W. Braunschweig, D. Husmann, K. Lübelsmeyer and D. Schmitz, Nucl. Phys. B **20**, 191 (1970).

[17] R. L. Anderson *et al.*, Phys. Rev. D **4**, 1937 (1971).

[18] T. E. Rodrigues, *O Modelo de Cascata Intranuclear Multi-Colisional e suas Aplicações para o Estudo do Mecanismo do Quase-Dêuteron e da Fotoprodução de Pions em Energias Intermediárias e Altas*, PhD thesis, IFUSP, University of São Paulo (2005).

[19] W. T. Meyer *et al.*, Phys. Rev. Lett. **28**, 1344 (1972).

[20] T. de Forest, Jr., Nucl. Phys. **A392**, 232 (1983).

[21] L. Lapikás *et al.*, Phys. Rev. C **61**, 064325 (2000).

[22] J. Mougey, *et al.*, Nucl. Phys. **A262**, 461 (1976).

[23] M. Bernheim et al., Nucl. Phys. **A375**, 381 (1982).

[24] K. Nakamura, S. Hiramatsu, T. Kamae, H. Muramatsu, N. Izutsu, and Y. Watase, Nucl. Phys. **A268**, 381 (1976).

[25] G. van der Steenhoven, H. P. Blok, E. Jans, M. De Jong, L. Lapikás, E. N. M. Quint, and P. K. A. De Witt Huberts, Nucl. Phys. **A480**, 547 (1988).

[26] T. H. Bauer, R. D. Spital, and D. R. Yennie, Rev. Mod. Phys. **50**, 261 (1978).

[27] Aachen-Berlin-Bonn-Hamburg-Heidelberg-München Collaboration, Phys. Letters **27B**, 474 (1968).

[28] J. Ballam *et al.*, Phys. Rev. Lett. **21**, 1544 (1968).

[29] C. A. Engelbrecht, Phys. Rev. **133**, B988 (1964).

[30] E. J. Moniz *et al.*, Phys. Rev. Lett. **26**, 445 (1971).

[31] I. Larin, A. Gasparian, L. Gan and S. Gevorgyan, *The π^0 background from ω and ρ mesons photoproduction in PRIMEX*, PrimEx note # 51 (2007).

[32] Robert J. Cence, *Pion-nucleon scattering*, Princ. Univer. Press, New Jersey, p.61 (1969).

[33] M. L. Perl, L. W. Jones, and C. C. Ting, Phys. Rev. **123**, 1252 (1963).

[34] K. J. Foley, S. J. Lindenbaum, W. A. Love, S. Ozaki, J. J. Russell, and L. C. L. Yuan, Phys. Rev. Lett. **11**, 425 (1963).

[35] K. J. Foley, R. S. Jones, S. J. Lindenbaum, W. A. Love, S. Ozaki, E. D. Platner, C. A. Quarles, and E. H. Willen, Phys. Rev. **181**, 1775 (1969).

[36] J. Cugnon, T. Mizutani, and J. Vandermeulen, Nucl. Phys. A **352**, 505 (1981); J. Cugnon, Nucl. Phys. A **462**, 751 (1987); J. Cugnon, C. Volant, and S. Vuillier, Nucl. Phys. A **620**, 475 (1997); A. Boudard, J. Cugnon, S. Leray, and C. Volant, Phys. Rev. C **66**, 044615 (2002); S. Leray *et al.*, Phys. Rev. C **65**, 044621 (2002); J. Benlliure *et al.*, Nucl. Phys. A **700**, 469 (2002); J. Cugnon and P. Henrotte, Eur. Phys. J. A **16**, 393 (2003).

[37] M. Effenberger, E. L. Bratkovskaya and U. Mosel, Phys. Rev. C **60**, 044614 (1999); J. Lehr, M. Effenberger, U. Mosel, Nucl. Phys. A **671**, 503 (2000).